J. Fluid Mech. (2025), *vol.* 1018, A9, doi:10.1017/jfm.2025.10504

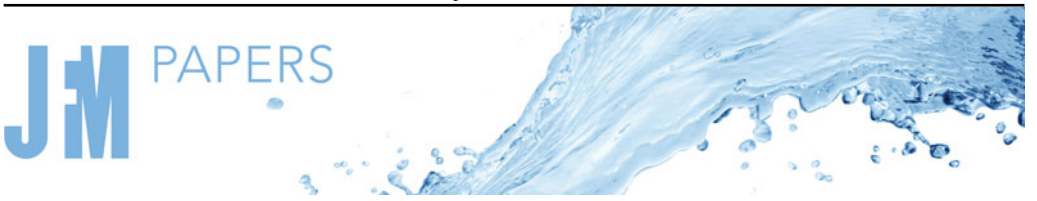

Shock-induced bubble jets: a dual perspective of bubble collapse and interfacial instability theory

Guillaume T. Bokman[1,2], **Luc Biasiori-Poulanges**[1], **Bratislav Lukić**[3], **Steven R. Brill**[2], **Claire Bourquard**[1,4], **Britton J. Olson**[2], **Alexander Rack**[3] and **Outi Supponen**[1]

[1]Department of Mechanical and Process Engineering, Institute of Fluid Dynamics, ETH Zurich, Sonneggstrasse 3, 8092 Zurich, Switzerland

[2]Lawrence Livermore National Laboratory, Livermore, CA 94550, USA

[3]ESRF – The European Synchrotron, Grenoble F-38043, France

[4]Dynamics & Control, Department of Mechanical Engineering, Eindhoven University of Technology, 5600 MB Eindhoven, The Netherlands

Corresponding author: Guillaume T. Bokman, bokmang@ethz.ch

(Received 21 February 2025; revised 11 June 2025; accepted 18 July 2025)

Interactions between shock waves and gas bubbles in a liquid can lead to bubble collapse and high-speed liquid jet formation, relevant to biomedical applications such as shock wave lithotripsy and targeted drug delivery. This study reveals a complex interplay between acceleration-induced instabilities that drive jet formation and radial accelerations causing overall bubble collapse under shock wave pressure. Using high-speed synchrotron X-ray phase contrast imaging, the dynamics of micrometre-sized air bubbles interacting with laser-induced underwater shock waves are visualised. These images offer full optical access to phase discontinuities along the X-ray path, including jet formation, its propagation inside the bubble, and penetration through the distal side. Jet formation from laser-induced shock waves is suggested to be an acceleration-driven process. A model predicting jet speed based on the perturbation growth rate of a single-mode Richtmyer–Meshkov instability shows good agreement with experimental data, despite uncertainties in the jet-driving mechanisms. The jet initially follows a linear growth phase, transitioning into a nonlinear regime as it evolves. To capture this transition, a heuristic model bridging the linear and nonlinear growth phases is introduced, also approximating jet shape as a single-mode instability, again matching experimental observations. Upon piercing the distal bubble surface, jets can entrain gas and form a toroidal secondary bubble. Linear scaling laws are identified for the pinch-off time and volume of the ejected bubble relative

to the jet's Weber number, characterising the balance of inertia and surface tension. At low speeds, jets destabilise due to capillary effects, resulting in ligament pinch-off.

Key words: bubble dynamics, nonlinear instability, jets

1. Introduction

The interaction of bubbles with pressure waves is a complex and dynamic multiphase process that occurs in a broad spectrum of hydraulic applications, including turbomachinery (Ligrani *et al.* 2020; Lui *et al.* 2022), materials processing and cleaning (Lauterborn & Vogel 2013; Mason 2016), therapeutic shock wave lithotripsy (Sackmann *et al.* 1988; Johnsen & Colonius 2008; Loske 2017), as well as biomedical ultrasound (Apfel 1982; Ohl, Klaseboer & Khoo 2015). Furthermore, shock waves inducing cavitation activity have been demonstrated to increase cell membrane permeability (Ohl *et al.* 2006; Le Gac *et al.* 2007), thereby promoting the transfer of foreign materials into cells in both *in vitro* and *in vivo* environments (Delius & Adams 1999; Zhong *et al.* 1999; Bekeredjian *et al.* 2007). When a shock wave interacts with a single bubble, the surrounding effective pressure jump acting on the bubble interface causes its rapid compression, which can eventually lead to its collapse under sufficiently strong shock pressures. This collapse generates intense localised pressures and strong subsequent shock waves (Plesset & Chapman 1971; Lauterborn & Bolle 1975; Shima, Tomita & Takahashi 1984; Johnsen & Colonius 2009) and can give rise to the formation of high-speed jets (Ohl & Ikink 2003; Freund, Shukla & Evan 2009) travelling in the direction of propagation of the shock wave. Jets with sufficient momentum can reach the far side of the bubble and re-enter the surrounding liquid (Speirs *et al.* 2018; Kroeze, Fernandez Rivas & Quetzeri-Santiago 2024), entraining gas that may detach as a toroidal bubble (Ohl & Ikink 2003; Kersten, Ohl & Prosperetti 2003). Micrometre-sized jets, in particular, demonstrate promising potential for applications in transdermal drug delivery, such as needle-free injections (Prausnitz, Mitragotri & Langer 2004; Quetzeri-Santiago *et al.* 2021). As the energy of the shock wave is reduced, the jets' speed also decreases (Philipp *et al.* 1993; Ohl & Ikink 2003; Bokman *et al.* 2023) which may make them prone to capillary-driven surface instabilities. The Rayleigh–Plateau instability for semifinite ligaments as been investigated for its relevance in technologies such as ink-jet printing, and the breakup dynamics of such ligaments are generally referred to as end-pinching (Culick 1960; Stone & Leal 1989; Castrejón-Pita *et al.* 2012; Paré 2015). As the intensity of the shock is further decreased, no jets are observed and the bubble oscillates linearly, which marks the limit of jetting. Varying peak pressure thresholds for jetting onset have been reported in the past but show significant and unexplained differences between studies (Ding & Gracewski 1996; Ohl & Ikink 2003; Bokman *et al.* 2023).

Gaining a fundamental understanding of the physics governing shock-bubble dynamics at the level of an individual bubble is essential for effectively managing and enhancing these interactions in applications where bubble jets are required on demand. Previous studies have explored shock–bubble interactions through both experimental (Philipp *et al.* 1993; Kodama & Takayama 1998; Ohl & Ikink 2003; Wolfrum *et al.* 2003; Abe *et al.* 2015) and numerical approaches (Ding & Gracewski 1996; Klaseboer *et al.* 2007; Calvisi *et al.* 2007; Johnsen & Colonius 2008; Freund *et al.* 2009; Johnsen & Colonius 2009; Kobayashi, Kodama & Takahira 2011; Betney *et al.* 2015; Koukas, Papoutsakis & Gavaises 2023). The interaction of gas bubbles with underwater pressure waves is often studied using cavitation theory, or bubble collapse theory, where a bubble initially at rest is driven by an external acoustic wave, such as ultrasound (Brenner, Hilgenfeldt & Lohse 2002)

or shock waves (Wolfrum *et al.* 2003; Johnsen & Colonius 2008, 2009; Ohl *et al.* 2015). In this approach, the bubble dynamics is effectively described by the Rayleigh–Plesset (Plesset 1949) or Keller–Miksis (Keller & Miksis 1980) equations. The collapse time of bubbles, τ_c, measured from the passage of the shock wave to the moment when the bubble reaches its minimum size, can be accurately estimated using the Keller–Miksis equation (Philipp *et al.* 1993; Wolfrum *et al.* 2003; Abe *et al.* 2015). For shock waves of infinite duration and sufficient amplitude, the collapse time scales with the Rayleigh collapse time (Rayleigh 1917; Johnsen & Colonius 2009), while for impulsive shock waves it is better described by the impulsive collapse time (Bokman *et al.* 2023). However, the study of bubble jets (Philipp *et al.* 1993; Kodama & Takayama 1998; Ohl & Ikink 2003) remains challenging due to experimental limitations for visualising the jet formation and propagation within the bubble using conventional imaging techniques such as shadowgraphy. Numerical studies of jets have largely focused on strong shock waves, exhibiting an infinitely long sustained pressure amplitude (Johnsen & Colonius 2009; Betney *et al.* 2015) or decaying pressure amplitude over a long duration (Johnsen & Colonius 2008; Koukas *et al.* 2023), with limited research on lower peak pressures involving impulsive, short-duration shock waves often encountered in experiments (Tomita & Shima 1986; Philipp *et al.* 1993; Ohl & Ikink 2003; Wolfrum *et al.* 2003; Tagawa *et al.* 2016; Bokman *et al.* 2023). This occurs primarily because shock waves reverse their polarity upon reflecting at the bubble wall due to the lower impedance of air compared with water. This phenomenon presents a challenge for many numerical codes, particularly when the incident shock wave is too short to prevent the liquid from experiencing tension. As a result, most insights into jetting phenomena rely on empirical and averaged models (Philipp *et al.* 1993; Ohl *et al.* 2015; Bokman *et al.* 2023), and the exact origin and conditions necessary for jet formation in shock-driven bubble collapses remain unclear.

Beyond the framework used to describe the interaction of bubbles with underwater shock waves through cavitation theory, several studies have suggested that the shock-driven dynamics of soap bubbles in air may be linked to acceleration-induced instabilities, such as the Rayleigh–Taylor and Richtmyer–Meshkov instabilities (Richtmyer 1954; Kull 1991; Brouillette 2002; Zhai *et al.* 2018), which arise from generally constant and shock-driven impulsive accelerations, respectively. Kelvin impulse-driven jets for vapour bubbles in water can be driven by constant acceleration, e.g. gravity (Supponen *et al.* 2016), suggesting a Rayleigh–Taylor-type of instability (Plesset & Mitchell 1956). Other studies have explored the dynamics of gas-filled soap bubbles interacting with shock waves in air-filled shock tubes (Rudinger & Somers 1960; Davy & Blackstock 1971; Haas & Sturtevant 1987; Ranjan *et al.* 2007; Layes, Jourdan & Houas 2009; Zhai *et al.* 2011), revealing complex three-dimensional effects that closely resemble the dynamics observed in underwater shock–bubble interactions. In such cases, the shock wave acts as a driving force that accelerates the interface between the bubble and the surrounding fluid. These instabilities deform the bubble interface and, under certain conditions, lead to the formation of jets, similar to those observed in bubble collapse dynamics in water. This connection was first highlighted by Dear, Field & Walton (1988), who studied the collapse of cylindrical cavities in a 12 % gelatine mixture triggered by shock waves generated by a striker (Bourne & Field 1992). They focused on the motion of the cavity's proximal side, approximating the interface motion by giving it a constant velocity equal to twice the particle velocity of the incident shock wave (Dear & Field 1988). The density contrast between the bubble gas and the surrounding liquid in which the shock wave is propagating is commonly characterised by the Atwood number, $A = (\rho_a - \rho_w)/(\rho_a + \rho_w) = -1.00$, where ρ_a and ρ_w stand for the densities of air and water, respectively. Research on acceleration-induced instabilities in bubbles, however, focus primarily on low or

positive Atwood numbers (Ranjan, Oakley & Bonazza 2011), and there remains room for improvement in the modelling of the corresponding experiments. Investigating Richtmyer–Meshkov instability for large density mismatches has become particularly relevant due to recent advances in nuclear fusion research (Betti & Hurricane 2016; Hurricane *et al.* 2023), especially in the field of inertial confinement fusion (ICF), where it plays an important role. An accurate understanding of this instability is critical, as it decreases the efficiency of ICF and is therefore undesirable (Haan 1991). Traditionally, these instabilities are investigated in two dimensions using single-mode or multimode perturbations to understand their growth and behaviour. Modelling the perturbation growth rate of a single mode (Liang *et al.* 2019), Richtmyer–Meshkov instability can be achieved with ranging accuracy through a wide spectrum of methods, such as numerically solving the linearised Euler equations (Yang, Zhang & Sharp 1994), employing analytical (Wouchuk 2001) or heuristic impulsive linear (Vandenboomgaerde, Mügler & Gauthier 1998) and nonlinear (Li & Zhang 1997; Sadot *et al.* 1998; Mikaelian 2008; Dimonte & Ramaprabhu 2010; Zhang & Guo 2016) models. The nonlinearities are important (Zhang & Sohn 1996; Sadot *et al.* 1998) because, above a certain level, they trigger saturation mechanisms of the growth rate relative to the linear rate and cause the perturbations to grow asymmetrically as bubbles and spikes for large Atwood numbers (Alon *et al.* 1995). Unfortunately, these models are limited to either early or late-time dynamics or are only applicable to a narrow range of Atwood numbers and do not perform well at large Atwood number and initial amplitude, which are characteristic of ICF and underwater shock–bubble interactions. In addition, there are compressibility (Velikovich *et al.* 2001), viscous and capillary effects (Mikaelian 1990; Carlès & Popinet 2002; Sohn 2009; Tang *et al.* 2021) that are fundamental to the Richtmyer–Meshkov instability and are difficult to model. The Richtmyer–Meshkov spikes found at $A = -1$, display similarities to jets, arising from the impulsive impact of liquid-filled containers on solid surfaces (Antkowiak *et al.* 2007; Eggers & Villermaux 2008; Gordillo, Onuki & Tagawa 2020), and bubble jets driven by shock waves and other types of instabilities, such as the Faraday wave instability (Zeff *et al.* 2000; Dhote *et al.* 2024).

In this study, underwater shock–bubble interactions are examined using X-ray phase contrast imaging, providing unprecedented visual access to the high-speed jets within and beyond the bubble. Here, Richtmyer–Meshkov theory is applied to a bubble collapse problem with $A = -1$, offering new insights into the jetting behaviour of bubbles interacting with laser-induced shock waves. Further understanding of the jet dynamics at the limit of jetting based on the acceleration of the bubble's proximal side during its collapse is gained, enabling better jet control based on initial shock intensities. In addition, the entry of micrometre-sized jets into the surrounding liquid is examined, which has potential applications in microinjections. The parameter range explored in this study builds on recent findings by Kroeze *et al.* (2024), enhancing the understanding of microjet control and application.

2. Experimental set-up

The shock-induced bubble dynamics is investigated using the experimental set-up depicted in figure 1(*a*). Air bubbles having an initial radius $r_0 = 380 \pm 38$ μm (number of specimens, $N = 41$) are generated at the bottom of a $100 \times 100 \times 350$ mm^3 water tank using a microfluidic device, comprising a PEEK low-pressure Tee connector with a 1 mm through-hole (P-714, IDEX) connected to a glass capillary (0.7 mm inner diameter, 100 mm length), which facilitates the discharge of bubbles into the deionised water-filled tank. Air is injected from the side, and water is provided from the bottom. The air flow, controlled by an air compressor (Fatmax DST 101/8/8 Bar, Stanley) and precision

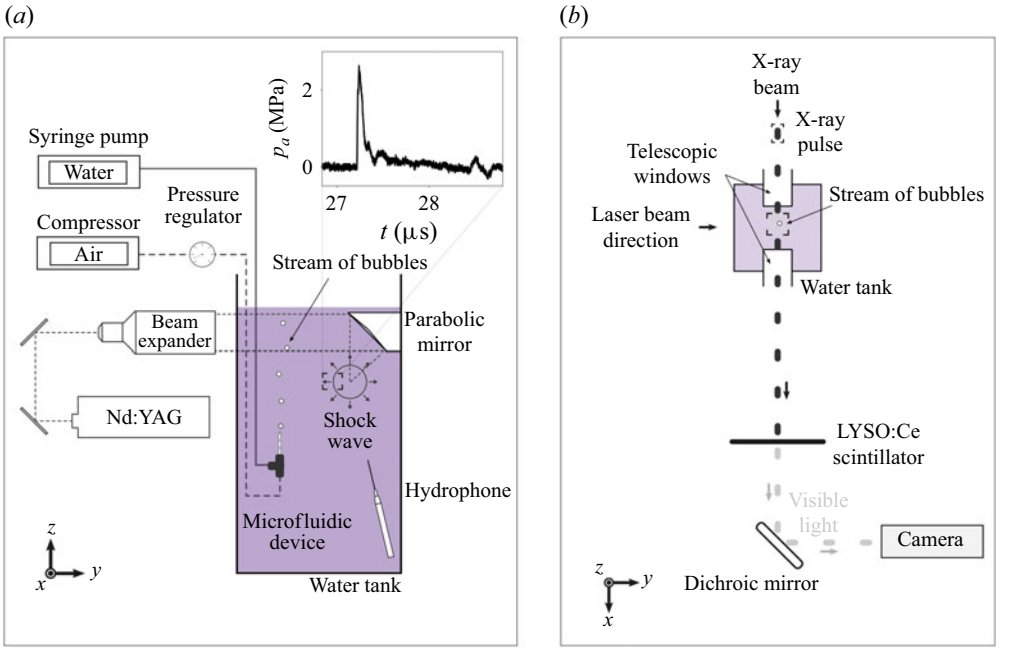

Figure 1. (*a*) Side view schematic of the experimental set-up. The inset shows the experimentally recorded pressure wave form of the shock wave, where p_a is the acoustic pressure and $t = 0$ μs corresponds to the moment of shock inception. (*b*) Top view of the X-ray beamline and imaging system of the ID19 at the ESRF.

pressure regulator (RP1000-8G-02, CKD), and the water flow, controlled by a syringe pump (Pump 33 DDS Dual Drive System, Harvard apparatus), result in a consistent production of bubbles when providing a constant water flow rate of 3.5 mL min^{-1} and by slowly letting air through the pressure regulator.

Shock waves are generated in water by optical breakdown. A 6 mm diameter laser pulse is provided by a Nd-YAG laser (Q-smart, 532 nm, 220 mJ, 5 ns, Lumibird), expanded by a 10× beam expander and refocused into a single point by a 90° parabolic mirror (Aluminium Off-Axis Mirror, Edmund Optics) fixed on the tank wall. The shock wave's origin is 5–7 mm away from the stream of bubbles. A needle hydrophone (NH0075, Precision Acoustics) measures the pressure waveform (see inset of figure 1*a*) 40.5 mm away from the shock origin and is recorded by an oscilloscope (WaveRunner 9000, Teledyne LeCroy). The peak pressure and pressure impulse are extrapolated to the bubble location, with ranges of 15.23–44.27 MPa and 1.05–3.36 Pa s, respectively. The complete methodology to assess the pressure at the bubble location can be found in Bokman *et al.* (2023). Note that, although the peak pressures are relatively low compared with those generated by explosive or ballistic sources, and a strict classification based on corresponding Mach number computed through Rankine–Hugoniot jump conditions might suggest an acoustic regime, as seen in table 1, the waves exhibit steep, nonlinear fronts with rapid rise times, key features of shock waves. Following convention in previous studies (Tomita & Shima 1986; Philipp *et al.* 1993; Ohl & Ikink 2003; Wolfrum *et al.* 2003; Johnsen & Colonius 2008), they are referred to as shock waves.

In situ high-speed synchrotron-based X-ray phase contrast imaging, providing optical access to all phase discontinuities along the X-ray beam path, allows the observation of the shock-induced bubble dynamics, including the internal jet structure. Radiographs are captured at the European Synchrotron Radiation Facility's (ESRF) 150 m long ID19

	Peak pressure	Temporal full width at half maximum	Pressure impulse	Dimensionless pressure impulse	Mach number
	p_{max} (MPa)	δ (ns)	j (Pa s)	$J/(r_0^3\sqrt{p_{b,0}\rho})$ (–)	M
(a)	42.98	40.77	3.36	10.40	1.05
(b)	42.19	41.30	2.70	8.62	1.05
(c)	36.79	39.45	2.17	6.72	1.05
(d)	27.67	40.24	1.62	5.03	1.05
(e)	22.27	38.65	1.14	3.48	1.04

Table 1. List of the driving shock wave parameters corresponding to the bubble dynamics of figure 2(a–e).

beamline. The polychromatic hard X-ray beam, with a mean energy of 30 keV, is produced using two axially aligned long-period undulators and is conditioned with a series of filters and in-vacuum slits along the vacuum flight tube to moderate the heat load delivered to the water tank in the experimental hutch. Figure 1(b) illustrates the X-ray beam passing through the custom-made water container, designed to minimise X-ray absorption using telescopic windows (SM1L10, Thorlabs). These windows can slide along the axis of the X-ray beam, and the inter-window distance is set to 20 mm to prevent excessive water absorption that would impede the detection of the transmitted signal. The X-ray beam is converted into visible light using a 500 µm thick LYSO:Ce scintillator. A dichroic mirror redirects the visible light to an ultra-high-speed Shimadzu Hyper Vision HPV-X2 camera. The camera, equipped with 4× magnification (8 µm/pixel), operates at a frequency of 0.5 Mfps and an exposure time of 1460 ns. The detector set-up is positioned 7.5 m downstream of the water container to ensure sufficient X-ray phase contrast through free-space propagation. This set-up enhances edge contrast due to partial spatial coherent illumination, while preserving the bubble shape in the images (Cloetens *et al.* 1996; Wilkins *et al.* 1996). The small dimensions of the water container and the inter-window gap cause bubbles to be influenced by reflections of shock waves and expansion waves from the boundaries. For a shock wave propagating near Mach one, the first reflections from the windows and container are expected to affect a bubble located at the centre of the set-up slightly before 14 µs and 68 µs, respectively. Due to the dispersion and dissipation of the shock waves in water, these reflections are considered secondary in influence. However, sufficient shock intensity is only achieved by locating the bubbles relatively close to its origin. The laser-induced breakdown at the origin of the shock wave also creates a vapour bubble that grows in the wake of the shock waves, inducing a radial pressure and velocity field around it. The laser-induced shock wave drives the early bubble dynamics, but the rebound is affected by the vapour bubble-induced pressure and velocity fields. The effects of both fields can be assessed using cavitation theory. A radial velocity field reaching a maximum value of $u_v = 1.06$ ms^{-1} is expected to flow in the direction of propagation of the shock wave at the location of the bubble, slightly increasing the jet speed. The pressure field at the bubble location is expected to reach values down to $p_v = 58.22$ kPa, which will cause the bubble to expand by an additional 49% during the rebound, assuming an adiabatic expansion of the air within the bubble. More details on the experimental system are provided in Bokman *et al.* (2024).

3. Results and discussion

When a shock wave interacts with a bubble, it converts acoustic energy into bubble motion. The high pressure difference induced by the shock wave at the bubble interface causes a

rapid compression of the bubble. The time delay required for the shock wave to travel along the bubble span causes its distal side to experience the pressure later, leading to a delayed and asymmetrical compression. If the shock wave is sufficiently strong, the initially spherical bubble can collapse asymmetrically and its proximal side can even evolve into a high-speed jet. Figures 2(*a–e*) display experimental image sequences of air bubbles having initial radii close to 400 μm, interacting with shock waves whose parameters are summarised in table 1. The bubbles are characterised by their initial radius, r_0, and initial pressure, $p_{b,0} = p_0 + 2\gamma/r_0$, made of the ambient pressure, $p_0 = 101\,325$ Pa, and Laplace pressure jump, where $\gamma = 72.8\ \mathrm{N\,m^{-1}}$ is the surface tension of water. The density of water is $\rho = 998\ \mathrm{kg\,m^{-3}}$. The flow equation can be non-dimensionalised by characteristic quantities built from these variables, yielding the bubble characteristic time, $r_0\sqrt{\rho/p_{b,0}}$, bubble characteristic speed, $\sqrt{p_{b,0}/\rho}$ and bubble characteristic momentum, $r_0^3\sqrt{p_{b,0}\rho}$ (Bokman *et al.* 2023). The impulse applied to the bubble surface, $J = 4\pi r_0^2 j$, where $j \approx \int p_a\,\mathrm{d}t$ is the shock wave pressure impulse, can be computed and normalised to the characteristic momentum of the bubble, yielding $J/(r_0^3\sqrt{p_{b,0}\rho}) = 3.48$–$10.40$. The shock wave travels from left to right and makes contact with the bubble at $t/(r_0\sqrt{\rho/p_{b,0}}) = 0$, the time normalised to the characteristic time of the bubble. The first image sequence in figure 2(*a*) shows an example of the strongest bubble dynamics observed in the present work. Following its interaction with the shock wave, the bubble collapses asymmetrically, compressing the air and reaching its minimum size at $t/(r_0\sqrt{\rho/p_{b,0}}) = 0.45$. The highly compressed gas causes the bubble to go through a rebounding phase, where the gas can expand and the pressure relax. However, the proximal side, which has a higher momentum, evolves into a high-speed jet that continues travelling in the direction of propagation of the shock wave, as observed in the third frame of figure 2(*a*). During the collapse of the bubble, the bubble surface typically flattens, temporarily losing its spherical or hemispherical shape. Jet formation occurs right after the bubble has reached its minimal size, when a sharp, narrow liquid protrusion penetrates into the bubble from one side, marked by a distinct, pointed structure emerging within the bubble. The jet adopts a conical shape, with its base keeping a constant radius and its tip becoming narrower as the jet elongates. The jet travels within the bubble and eventually pierces the distal side at $t/(r_0\sqrt{\rho/p_{b,0}}) = 0.80$, entraining some of the gas with it as it penetrates the surrounding liquid. The base of the gaseous protuberance starts necking as the jet continues propagating and pulling on the surrounding gas. Finally, a toroidal daughter bubble detaches from the main air bubble at $t/(r_0\sqrt{\rho/p_{b,0}}) = 2.15$ as the neck yields to surface tension forces. While the cylindrical torus, which has an inner radius approximately equal to a third of its outer radius, continues to travel within the liquid, the interface deforms. These deformations are likely due to surface waves emitted at the rupture of the interface as well as external shear stresses as the gas decelerates within the liquid. The main body of the bubble stays as a large torus with the jet connecting the proximal to distal side of the bubble. The response of the rupturing of the interface on the distal side of the bubble can be seen as a surface wave penetrating the inner cylinder of the torus at $t/(r_0\sqrt{\rho/p_{b,0}}) = 3.65$.

Figure 2(*b,c*) displays similar behaviour to that already described, although a reduced driving pressure hinders the intensity of the bubble dynamics. With weaker shock waves, the collapse is slower, the bubble compression milder and the proximal side deforms less. The bubble rebound is also smaller and the jet speed lower. Consequently, the jet entrains less gas as it pierces the distal bubble side and the volume and speed of the ejected toroidal bubble decrease while travelling within the surrounding liquid. Figure 2(*d*) shows a bubble interacting with a shock wave having a dimensionless pressure impulse of $J/(r_0^3\sqrt{p_{b,0}\rho}) = 5.47$, right below the empirical jetting limit of $J/(r_0^3\sqrt{p_{b,0}\rho}) = 6$

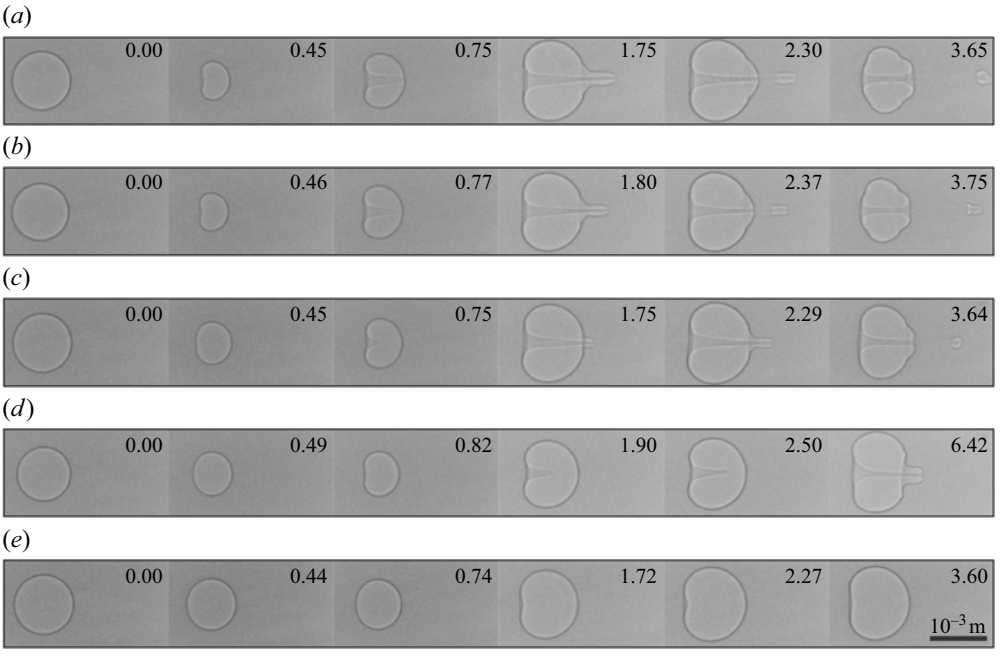

Figure 2. Image sequence of the dynamics of an air bubble interacting with a shock wave travelling from left to right, of dimensionless pressure impulse of $J/(r_0^3\sqrt{p_{b,0}\rho})$: (*a*) 10.40, (*b*) 8.62, (*c*) 6.72, (*d*) 5.03 and (*e*) 3.48. The dimensionless time, $t/(r_0\sqrt{\rho/p_{b,0}})$, is indicated on each frame and zero is the time at which the shock contacts the bubble. The scale bar is the same for all image sequences.

previously reported in Bokman *et al.* (2023). Here, the use of X-ray phase contrast imaging reveals a jet within the bubble at the jetting limit, which has never been observed using conventional imaging. However, due to its weaker momentum, the jet softly impacts the distal side of the bubble and no daughter bubble is ejected from the main bubble. Finally, in figure 2(*e*), the pressure impulse is too weak to induce jetting and, although the proximal side of the bubble does flatten and becomes slightly concave during the rebound, the bubble only oscillates linearly within the liquid.

The spatiotemporal evolution of the jets can be drawn by tracking their tip over time. Before the jet has formed and after it pierces the bubble's distal side, the proximal side of the bubble and the tip of the entrained gas are herein also defined as the jet tip. In figure 3(*a*), the location of the jet tip, z_j, normalised to the bubble's initial radius, r_0, is displayed with respect to dimensionless time for shock waves of varying intensity, characterised by their dimensionless pressure impulse applied to the bubble, $J/(r_0^3\sqrt{p_{b,0}\rho})$. The jet speed, u_j, is obtained by temporal differentiation of the location of its tip and is displayed in figure 3(*b*), normalised to the bubble's characteristic speed, $\sqrt{p_{b,0}/\rho}$. For $J/(r_0^3\sqrt{p_{b,0}\rho}) > 5$, the time evolution of the jet is clearly nonlinear with an initial acceleration phase during the collapse of the bubble $t/(r_0\sqrt{\rho/p_{b,0}}) < 1$ followed by a more or less linear evolution of the jet once it has breached the distal side of the bubble and travels within the surrounding liquid. The speed increases linearly during the collapse, reaching its maximum value at the moment the interface adopts a concave shape and a jet starts being visible. The maximum speed experimentally recorded for $J/(r_0^3\sqrt{p_{b,0}\rho}) > 5$ is found to be in the range $u_j/\sqrt{p_{b,0}/\rho} = 2.1$–$4.9$. Once the jet has formed, its speed decreases and settles to an approximately constant value corresponding to its cruising speed within the surrounding liquid, $u_j/\sqrt{p_{b,0}/\rho} = 0.5$–$1.2$. For $J/(r_0^3\sqrt{p_{b,0}\rho}) \approx 6$,

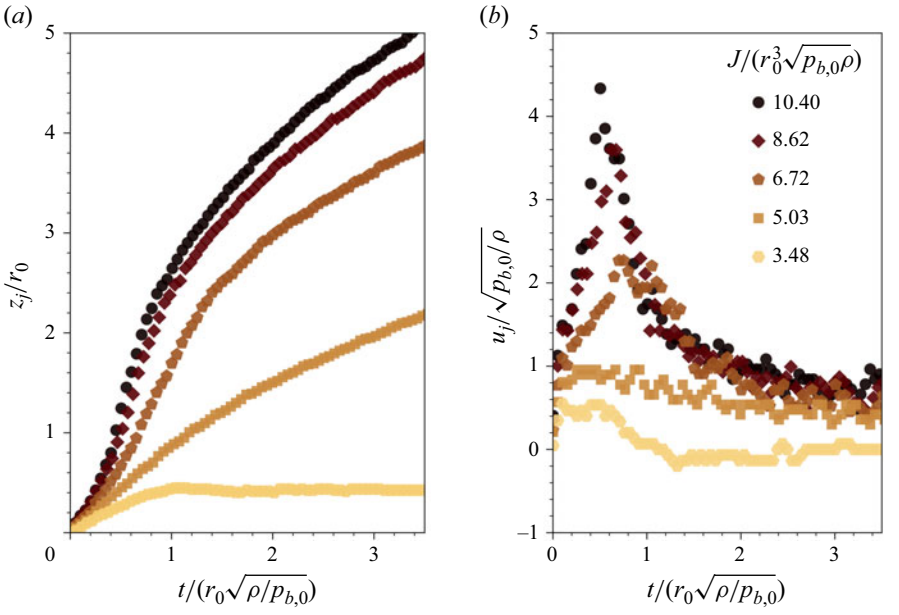

Figure 3. Time evolution of (*a*) the jet tip location, z_j, and (*b*) speed, u_j. The location, z_j, speed, u_j, and time, t, are normalised to the initial radius of the bubble, r_0, and the bubble characteristic speed and time, $\sqrt{p_{b,0}/\rho}$ and $r_0\sqrt{\rho/p_{b,0}}$, respectively.

corresponding to the limit for piercing jets, the spatiotemporal evolution of the jet is linear and the corresponding speed stays roughly constant after an initial brief acceleration phase. Lower pressure impulses display a simple linear evolution of the jet location during the collapse up to $t/(r_0\sqrt{\rho/p_{b,0}}) \approx 1$ where no jet forms and the jet tip stagnates. The speed of the bubble interface under such cases displays a short constant acceleration during the linear collapse of the bubble before converging to zero as expected by the stagnating jet tip. Here, the unprecedented visual access to the jets through their entire lifetime yields valuable information to help understand the mechanism behind jet formation.

3.1. *Bubble collapse-based approach*

The formation of a liquid jet following the passage of a shock wave has been observed only in cases of strong nonlinear bubble collapse (Bokman *et al.* 2023), typical of inertial cavitation, rather than during the linear oscillations that occur in so-called 'stable cavitation' (Petit *et al.* 2015) and driven by weaker shocks. This suggests that the onset of jetting depends on the nature of the bubble collapse. It is therefore insightful to examine the spatiotemporal evolution of the jet tip during the bubble collapse (i.e. before the appearance of the jet), in figure 4(*a*). The jet tip location is plotted with respect to time for five different shock wave impulses. The temporal evolution of the jet tip adopts a convex distribution for $J/(r_0^3\sqrt{p_{b,0}\rho}) > 5$, and a concave distribution for $J/(r_0^3\sqrt{p_{b,0}\rho}) < 5$. In between, the temporal evolution of the jet tip is linear. These results suggest that the jet's motion follows a quadratic evolution over time:

$$z_j(t) = a_j t^2 + u_{j,0} t + z_{j,0}, \tag{3.1}$$

where, a_j, is the effective mean and constant acceleration of the jet, $u_{j,0}$, the initial velocity jump induced by the shock wave and $z_{j,0}$ the initial location of the jet. The acceleration of

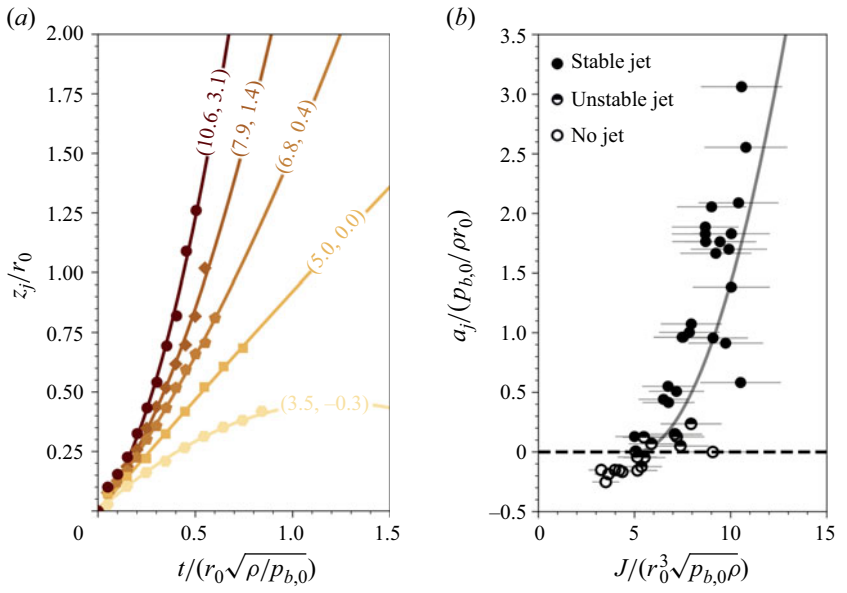

Figure 4. (*a*) Time evolution of the jet tip location during the bubble collapse. The dimensionless impulse and acceleration of the jet are indicated in brackets for each curve $[J/(r_0^3\sqrt{p_{b,0}\rho}), a_j/(p_{b,0}/\rho r_0)]$. (*b*) Dimensionless acceleration of the jet tip during the collapse phase of the bubble against the dimensionless pressure impulse of the shock wave applied to the bubble surface. The dashed dark line indicates the jetting limit for $a_j/(p_{b,0}/\rho r_0) \approx 0$ and the grey curve shows the scaling law in (3.4).

the jet as well as its initial velocity, induced by the impulsive effect of the shock wave impact, can be extracted from the radiographs. However, to minimise the uncertainty propagation from the first and second derivative of the jet tip's displacement, both values are fitted to the trajectory of the jet and verified to be well within the experimental uncertainty. The best fit of (3.1) is performed for the acceleration and jump velocity for each case, assuming $z_{j,0} = 0$ at the moment the shock impacts the proximal side of the bubble, and displayed as solid curves in figure 4(*a*). All convex curves correspond to bubbles exhibiting a stable jet that pierces their distal side and are characterised by a positive acceleration of the jet tip $a_j > 0$. The pressure driving corresponding to a linear curve is close to the (previously mentioned) empirical jetting limit, and unsurprisingly, the acceleration is close to zero and the jet exhibits an unstable behaviour, which will be discussed later. For a negative acceleration, no jet is observed. For each curve, the pressure impulse and jet tip acceleration are displayed in dimensionless form using the bubble's characteristic momentum and acceleration, $p_{b,0}/\rho r_0$, respectively.

The results are presented in figure 4(*b*), where the jet tip acceleration, a_j, is plotted against the pressure impulse. For cases where stable bubble jetting occurs, the acceleration is positive, with values in the range $a_j/(p_{b,0}/\rho r_0) = 0$–3.1. At the jetting threshold, where jets are unstable, the dimensionless acceleration approaches zero, while for non-jetting bubbles, it is negative, ranging from $a_j/(p_{b,0}/\rho r_0) = -0.3$–0. As expected, a positive acceleration is necessary to generate sufficient momentum for the proximal side of the bubble to evolve into a stable jet, overcoming the 'pulling' force from the rebound of the gas phase and the surface tension effects. The acceleration is expected to show a quadratic dependence on the pressure impulse, consistent with the inverse relationship between the impulsive mean jet speed and the impulsive collapse time (Bokman *et al.* 2023), $u_j \propto \tau_c^{-1}$,

given that the collapse time inversely scales with the impulse, $\tau_c \propto J^{-1}$, and acceleration is the first derivative of velocity. This relationship can be obtained by assuming that the jet acceleration scales with the mean jet speed, $u_j = Cr_0/\tau_c^{-1}$, where $C = 1.43$ is a fitted constant, leading upon dimensional considerations to

$$a_j = \frac{Cr_0}{\tau_c^2}, \tag{3.2}$$

where the impulsive collapse time is defined as (Bokman *et al.* 2023)

$$\frac{\tau_c}{r_0\sqrt{\rho/p_{b,0}}} = \frac{8\pi}{5}\left(\frac{J}{r_0^3\sqrt{p_{b,0}\rho}}\right)^{-1}. \tag{3.3}$$

Substituting this into (3.2) yields

$$\frac{a_j}{p_{b,0}/\rho r_0} = C\frac{25}{64\pi^2}\left(\frac{J}{r_0^3\sqrt{p_{b,0}\rho}}\right)^2. \tag{3.4}$$

The equation describes the amplitude of the mean acceleration of the jet as a function of the pressure impulse and is found to scale well with that found for jetting bubbles (i.e. $J/(r_0^3\sqrt{p_{b,0}\rho}) \geqslant 5$) as indicated by the grey curve displayed in figure 4(*b*). This scaling is, however, only valid for bubbles that produce a jet.

3.2. *Acceleration-induced interfacial instability-based approach*

The acceleration of the proximal side of the bubble during collapse is a key factor in determining whether a jet will form. Acceleration-driven interfacial instabilities, such as the Rayleigh–Taylor and Richtmyer–Meshkov instabilities, which are classically associated with sustained and impulsive acceleration, respectively, may play a central role in this process. However, due to the complex interplay between the shock wave, bubble collapse and jet formation, it remains unclear to the authors whether the jet originates from one of these instabilities alone or from a more intricate coupling between multiple mechanisms.

The shock wave in itself could potentially induce the Richtmyer–Meshkov instability. However, the pulse generated in the present configuration is of very short duration with respect to the jetting dynamics and is immediately followed by an exponential decay as observed in figure 1(*a*), yielding an effective pressure profile characteristic of a blast wave. This inversion of the pressure gradient after the peak of the shock wave may rapidly reverse the vorticity deposited by the initial shock front, potentially cancelling the Richtmyer–Meshkov growth in its earliest stages. Moreover, blast-wave-driven interfacial instability studies have postulated that the deceleration caused by the rarefaction could induce Rayleigh–Taylor growth coupled to Richtmyer–Meshkov effects (Kuranz *et al.* 2009; Drake 2011). Assessing which of these competing effects dominates is difficult, as they occur within the first few frames of the experiment.

Additionally, the passage of the shock wave causes the bubble to collapse and rebound, effectively accelerating its interface. The stability of bubbles to non-spherical disturbances has been analysed using a model analogous to the spherical Rayleigh–Taylor instability (Birkhoff 1954; Plesset & Mitchell 1956). One common approach to modelling the dynamics of non-spherical bubbles involves expanding the interface perturbation in terms of spherical harmonics. While this method offers certain advantages, Plesset & Prosperetti (1977) noted that it is neither the only approach nor the most practical in all situations. Although mathematically elegant, this method becomes challenging to apply in the context

of bubbles interacting with laser-induced shock waves, due to the inherently non-uniform and asymmetric nature of the shock-induced collapse. These complexities make it difficult to define an appropriate initial interface shape and velocity distribution, as well as to track the interface acceleration throughout the collapse. In this model, the mean radius, its velocity and acceleration are typically modelled using Rayleigh–Plesset or Keller–Miksis-type equations. Such equations indicate that during the shock passage and the early stage of collapse, the interface acceleration is directed inward, toward the bubble centre. Before the bubble reaches its minimum volume, the acceleration is directed outward, toward the surrounding liquid. This configuration renders the interface most susceptible to Rayleigh–Taylor instability (Brennen 2014). After its collapse, the bubble re-expands, and toward its maximum size, the direction of acceleration reverses once more, in the direction of the bubble centre, thereby stabilising the interface. A comprehensive analysis of this dynamic Rayleigh–Taylor instability behaviour lies beyond the scope of the present work.

This study presents a brief attempt to model the jet tip dynamics as the growth of an initial simple perturbation, through a Richtmyer–Meshkov instability initiated by the shock wave. Due to the complexity of the underlying dynamics, simplified linearised models are employed. More accurate approaches, such as Layzer-type models (Layzer 1955), based on potential flow theory could, in principle, offer a more precise approximation of the evolving jet tip (Zhang 1998; Mikaelian 2014; Zhou 2017). However, such models also fall outside the scope of the present analysis and are reserved for future investigation. The linearised models adopted here serve as foundational tools for providing a simplified interpretation of jet formation in bubbles subjected to laser-induced shock waves.

A single-mode perturbation in the context of acceleration-driven interfacial instabilities refers to the study of instability growth that originates from a disturbance or perturbation with a single, well-defined wavelength or frequency at the interface between two fluids of different densities. For a single-mode perturbation, this growth manifests as a regular, predictable pattern, such as a single sinusoidal wave that becomes progressively amplified over time. The study of acceleration-driven interfacial instabilities with single-mode perturbations provides a simpler framework to understand the fundamental mechanisms of instability growth, including the development of characteristic ‘spikes’ (penetrations of the heavier fluid into the lighter fluid) and ‘bubbles’ (penetrations of the lighter fluid into the heavier fluid). Here, considering the jet (or spike) to arise from a perturbation, η, the perturbation growth rate can be computed based on a simple approach presented in figure 5(*a*) and first proposed by Haas & Sturtevant (1987). For simplicity, the bubble interface is assumed to be a quasi-single-mode perturbation (Liang *et al.* 2019). The real part of the perturbation is initially described as

$$\begin{aligned} \eta(x, 0, 0) &= \mathrm{Re}\left[\eta_0 \exp\left(ik_x x\right)\right] = \eta_0 \cos(k_x x), \\ \eta(0, y, 0) &= \mathrm{Re}\left[\eta_0 \exp\left(ik_y y\right)\right] = \eta_0 \cos(k_y y), \end{aligned} \tag{3.5}$$

in x and y, respectively. Haas & Sturtevant (1987) approximated the bubble interface by expressing the initial amplitude, η_0, and the wavenumber, k, of the perturbation as functions of the bubble radius,

$$\begin{aligned} \eta_0 &= r_0, \\ k_x &= \frac{1}{r_0}, \end{aligned} \tag{3.6}$$

as illustrated by the dashed sine wave in figure 5(*a*). These values are believed to offer a good approximation of the overall bubble dynamics in cases involving strong, sustained shock waves, as in the original study by Haas & Sturtevant (1987). However,

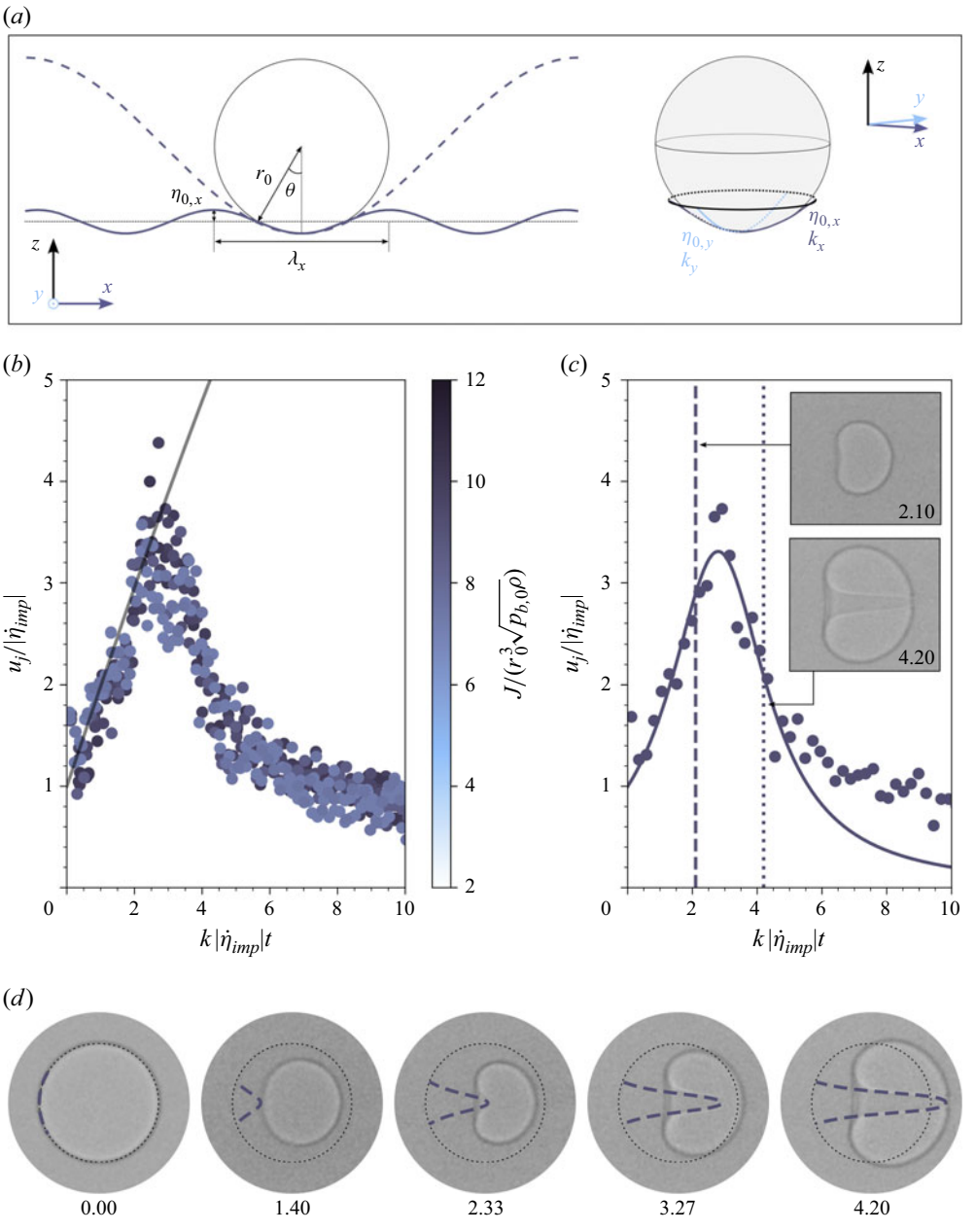

Figure 5. (*a*) Schematic drawing of the quasi-single-mode approximation of the bubble, defining the initial amplitude and wavelength of the initial perturbation. The dashed and full curves display the approximation proposed by Haas & Sturtevant (1987) and in the present work, respectively. (*b*) Time evolution of the jet speed for ten jetting bubbles driven by different shock waves. The jet speed and time are made dimensionless by the wavenumber, k, and impulsive perturbation growth rate in the sense of Richtmyer and Meshkov, $\dot{\eta}_{imp}$, and (3.9) is displayed in grey. (*c*) Comparison between a single test case and (3.11). The inset images show the bubble at its minimum size and when the jet reaches its distal side for the dimensionless times corresponding to the vertical dashed and dotted line, respectively. (*d*) Comparison between the theoretical prediction of the jet shape from (3.11) and the experiment for different non-dimensional times $k|\dot{\eta}_{imp}|t$. The initial bubble shape is indicated as a dotted circle.

this approximation tends to overestimate the resulting jet speed (Haas & Sturtevant 1987) and appears to be inadequate for capturing jets generated by laser-induced impulsive shock waves. Although the reason for this discrepancy remains unclear, the authors believe it may stem from the coupling between bubble collapse and jet formation. The angle θ used to define the jetting region, taken here as $\theta \in [-\pi/6, \pi/6]$, is selected empirically based on visual observations of the angular extent over which the jet structure develops consistently in experiments. Accordingly, the initial amplitude, η_0, and wavenumber, k, of the perturbation are defined as

$$\eta_0 = r_0[1 - \cos(\pi/6)] = \frac{(2-\sqrt{3})r_0}{2},$$
$$k_x = \frac{2\pi}{\lambda_x} = \frac{2\pi}{4r_0 \sin(\pi/6)} = \frac{\pi}{r_0}, \tag{3.7}$$

where λ is the single-mode wavelength. The problem is three-dimensional, as shown in figure 5(*a*), and the initial amplitude of the perturbation is taken to be identical in both the x and y directions; the wavenumbers satisfy $k_x = k_y$. Thus, the total wavenumber is given by $k = \sqrt{k_x^2 + k_y^2} = \sqrt{2}/r_0$ for Haas & Sturtevant (1987) and $k = \sqrt{2}\pi/r_0$ in the present work. These values of η_0 and k therefore represent the magnitudes of the initial wave perturbation in three dimensions (Zhang & Sohn 1999; Zhou *et al.* 2021).

Many models have been proposed to describe the perturbation growth rate in the sense of Richtmyer and Meshkov, $\dot{\eta}$, over time, starting from Richtmyer (1954) who suggested the impulsive growth rate of the perturbation to be constant over time:

$$\dot{\eta} = \dot{\eta}_{imp} = Ak\eta_0 u_{j,0}, \tag{3.8}$$

where $u_{j,0}$ is the velocity jump after the incident shock passage and A, k and η_0 are the post-shock quantities considered to be equal to the pre-shock conditions because of the impulsive and short nature of the laser-induced shock wave. An expansion of the flow equations to second order yields a linear relationship between the growth rate of the perturbation and time (Haan 1991; Alon *et al.* 1995; Zhang & Sohn 1996), in accordance with experimental observations displayed in figure 5(*b*), where the grey line is given by

$$u_j = \dot{\eta}(t) = |\dot{\eta}_{imp}| \left(1 + k|\dot{\eta}_{imp}|t\right). \tag{3.9}$$

Here, the speed and time are normalised to the wavenumber of the perturbation, k, and the magnitude of the impulsive growth rate of the perturbation in the sense of Richtmyer and Meshkov, $|\dot{\eta}_{imp}|$ (Zhang & Sohn 1996; Dimonte & Ramaprabhu 2010). An excellent agreement is found between the measured early jet speed and the predicted growth rate of the perturbation through the entire collapse of the bubble for ten different bubble–shock wave experiments as displayed in figure 5(*b*). In these cases, the bubble dynamics and jet are inertially driven with Weber numbers higher than 100 for both the bubble and the jet, so surface tension effects are negligible. Once the bubble has collapsed and starts re-expanding at $k|\dot{\eta}_{imp}|t > 2.10$, the jet fully forms and travels within the bubble, its speed decaying over time.

Only the early-stage dynamics of the perturbation are described by (3.9). To account for the later, nonlinear evolution of the perturbation, Li & Zhang (1997) introduced a three-dimensional nonlinear model that captures the perturbation growth rate of the Richtmyer–Meshkov instability

$$u_j = \dot{\eta}(t) = \frac{|\dot{\eta}_{imp}|}{1 + D_0\eta_0 k^2|\dot{\eta}_{imp}|D_1 t + \max(0,\, k^2\eta_0^2 D_1^2 - D_2)k^2|\dot{\eta}_{imp}|^2 t^2}, \tag{3.10}$$

where $D_0 = 1$ for a system with no phase inversion and $D_0 = -1$ for a system with phase inversion, i.e. negative amplitude is interpreted as a phase inversion (Yang *et al.* 1994). This nonlinear equation is obtained by developing the initial perturbation using a Taylor's series up to order three, followed by Padé approximants, which lead to the coefficients $D_1 = 0.54$ and $D_2 = 0.16$ for the Atwood number of the present work (Li & Zhang 1997). Here, the quasi-single-mode perturbation assumption leads to $k\eta_0 = 0.60$, which means that the second-order term in (3.10) is equal to zero and yields inconsistent results with regards to the jet speed evolution displayed in figure 5(*b*). However, a heuristic approach (Li & Zhang 1997; Sadot *et al.* 1998) suggests that the jet speed is adequately modelled as the growth rate of a Richtmyer–Meshkov perturbation by

$$u_j = \dot{\eta}(t) = \frac{|\dot{\eta}_{imp}|}{1 - E_1\eta_0 k^2|\dot{\eta}_{imp}|t + E_2\eta_0^2 k^4|\dot{\eta}_{imp}|^2 t^2}, \tag{3.11}$$

where $E_1 = 0.87 \pm 0.04$ and $E_2 = 0.27 \pm 0.03$ are fitted scaling constants found to be fairly consistent over the range of shock driving studied herein. The heuristic model matches the experimental data well during the bubble collapse, indicated by the vertical dashed line at $k|\dot{\eta}_{imp}|t = 2.10$, where the jet speed grows linearly and during the expansion of the bubble all the way up to the moment the jet contacts the distal bubble side, indicated by the vertical dotted line at $k|\dot{\eta}_{imp}|t > 4.20$, although it tends to underestimate the peak jet speed. For the range of experiments investigated herein, a single scaling constant can be used by setting $E_2 = \eta_0^2 k^2 E_1^2 \approx 0.27$, building on the relationship between the exponents used in (3.10).

Based on the heuristic approach proposed here (3.10), an approximation of the jet shape can be attempted by considering the full single-mode form $\eta = \eta_0 \cos(kx)$, rather than only its centre value $\eta = \eta_0$. The resulting theoretical jet shapes are compared with experimental observations in figure 5(*d*). Before the jet adopts a concave profile and penetrates into the bubble, only the jet tip aligns with experimental data, as seen for dimensionless times up to $k|\dot{\eta}_{imp}|t = 2.33$. However, once the jet begins to penetrate the bubble, the approximation yields a reasonable match within the limits of the linear framework employed. The remainder of the bubble interface, which is influenced by collapse and rebound dynamics, cannot be captured by this model. To improve accuracy, this approach should be combined with the Rayleigh–Plesset or Keller–Miksis equations to capture the radial dynamics, along with a model for predicting the translational motion of the bubble (Ohl 2002). Even so, spurious cusps are expected to appear at the junction between the bubble collapse solution and the jet shape described by (3.10), as previously noted by Dear *et al.* (1988), who also attempted to approximate cavity collapse under shock using a different linear framework.

3.3. *Jet breakup and end-pinching*

The shock-induced bubble jets evolve into a narrow bell-shaped structure during their propagation within the air bubble. Their shape can quickly be approximated by a quasi-cylindrical semifinite liquid ligament, whose dynamics is governed by inertial, surface tension and viscous forces. The velocity of the shock-induced bubble jets decreases with a decreasing shock wave impulse. Close to the jetting limit, capillary forces begin to overcome inertial ones, causing the jets to become unstable, which may cause the jet tip to break up into a small droplet as observed in figure 6(*a*). This capillary-driven instability for semifinite ligaments and their breakup dynamics, also known as end-pinching, are displayed in figure 6(*b*). At the tip of the jet, the inertial pressure of the liquid cannot balance the increase in pressure caused by the curvature of the interface, causing the

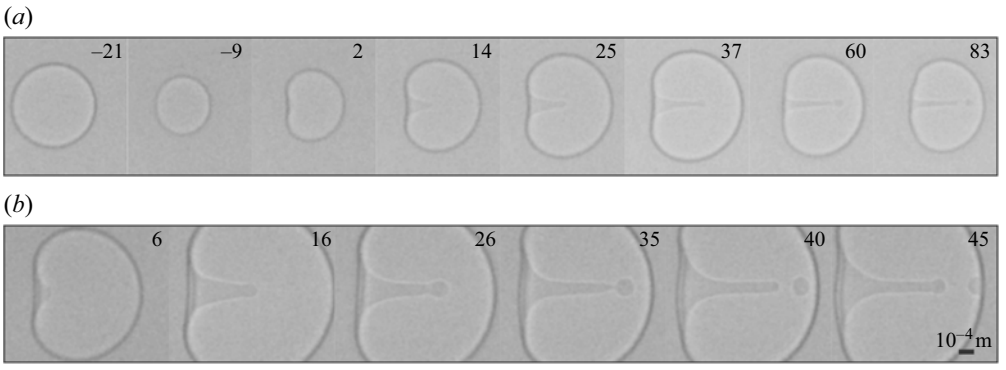

Figure 6. (*a*) Image sequence of the dynamics of an air bubble interacting with a shock wave travelling from left to right and having a pressure impulse of $J/(r_0^3\sqrt{p_{b,0}\rho}) = 7.87$. The subsequent end-pinching breakup of the liquid jet under capillary forces is observed. The normalised rescaled time, $\tilde{t}u_j(\tilde{t}=0)/r_j$, is indicated on each frame where $\tilde{t} = t - t_j = 0$ is the time at which the bubble becomes concave and a jet forms ($t_j = 18$ µs) and r_j and $u_j(\tilde{t}=0)$ the jet radius and initial jet speed. The jet's Weber number is $We_j = 46$. (*b*) Image sequence focusing on the end-pinching phenomenon of a larger shocked air bubble for a pressure impulse of $J/(r_0^3\sqrt{p_{b,0}\rho}) = 5.11$. The jet's Weber number is $We_j = 33$. The jet forms $t_j = 36$ µs after the passage of the shock wave. The scale bar is the same for both image sequences.

ligament to retract at a constant speed, called Taylor–Culick speed:

$$u_{TC} = \sqrt{\frac{\gamma}{\rho r_j}}, \tag{3.12}$$

where r_j is the radius of the cylindrical jet. This speed corresponds to ligaments at rest and is therefore relative to the jet motion here. The retraction of the jet due to capillary forces results in liquid accumulation in the form of a bulge at the tip, as observed in the third frame of figure 6(*b*). Eventually, the back flow creates a neck at the base of the bulge which collapses under the pressure jump associated with its curvature, leading to the separation of a drop at the jet's tip, as shown in the fourth and fifth frames of figure 6(*b*). Finally, the newly created drop travels towards the distal bubble side at a constant speed, while the end of the jet becomes unstable once more and a new protuberance associated with the end-pinching starts developing.

The spatiotemporal evolution of the jet is displayed in figure 7(*a*) from the time at which the bubble becomes concave and a jet forms, t_j. The time and position of the jet tip are rescaled as $\tilde{t} = t - t_j = 0$ and $\tilde{x}_j = z_j(t) - z_j(t_j) = 0$, respectively, and the initial jet speed $u_j(\tilde{t}=0)$ can be evaluated. The Weber numbers, $We_j = 2\rho r_j u_j^2(\tilde{t}=0)/\gamma$, are found to be in the 16–84 range. Upon spatial and temporal normalisation to the jet radius, r_j, and jet inertial characteristic time, $r_j/u_j(\tilde{t}=0)$, self-similarity is observed and the jet position is found to scale with time as

$$\frac{\tilde{x}_j}{r_j} = F\left(\frac{\tilde{t}u_j(\tilde{t}=0)}{r_j}\right)^{2/3}, \tag{3.13}$$

as indicated by the grey curve in figure 7(*a*), where $F = 1.82$ is an empirically determined scaling constant. A good agreement is found between all tests and (3.13), which describes the time evolution of inertia- and capillary-driven jets, with the exception of the test at $We_j = 16$, which diverges from the self-similar solution at $\tilde{t}u_j(\tilde{t}=0)/r_j = 10$. This is further illustrated by the superimposed bubble jet shapes shown in figure 7(*b*), corresponding to the tests in figure 7(*a*). While some variation in the bubble contours near

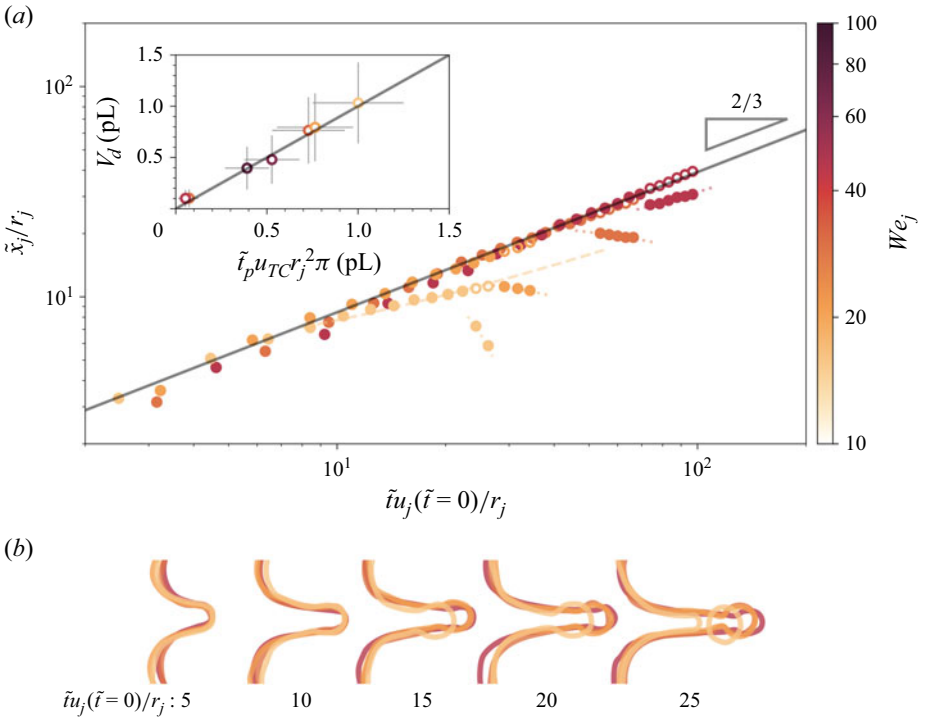

Figure 7. (*a*) Spatiotemporal evolution of the jet tip's location, normalised to the jet radius, from the moment the jet forms, $\tilde{t} = t - t_j$, normalised to the inertial time scale, $r_j/u_j(\tilde{t}=0)$. The drop and jet are displayed as open and closed markers, respectively. The solid, dashed and dotted curves correspond to (3.13) for $We_j > 1$, (3.14) for $We_j < 1$ and the evolution of the ejected drop position derived from the Taylor–Culick speed (3.12) relative to the jet speed at the drop pinch-off, $u_j(\tilde{t}_p) - u_{TC}$, respectively. The inset figure displays the ejected drop volume with respect to (3.15), representing the liquid volume that accumulates at the jet tip because of capillary forces. (*b*) Superimposition of the bubble jet contours corresponding to figure 7(*a*), illustrating selfsimilarity of their shape while in the inertia-capillary regime, for different dimensionless times.

the jet base arises from differences in the stages of collapse or expansion, the jet contours remain self-similar at each dimensionless time, except for minor discrepancies caused by liquid accumulation at the jet tip shortly before end-pinching, as well as the case with $We_j = 16$, which begins to deviate from $\tilde{t}u_j(\tilde{t}=0)/r_j = 10$. Indeed, as the jet evolves, its speed decreases because of viscous and capillary effects, which results in the jet's Weber number decreasing, eventually dropping below one, and capillary effects eventually becoming dominant. At that moment, non-dimensionalisation of the time must be switched from the inertial time scale to the capillary time scale $\sqrt{\rho r_j^3/\gamma}$,

$$\frac{\tilde{x}_j}{r_j} = F\left(\frac{\tilde{t}\sqrt{\gamma}}{\sqrt{\rho r_j^3}}\right)^{2/3}, \tag{3.14}$$

which captures well the deviation of the jet position as observed by the good agreement between the dashed curve and corresponding test case at $We_j = 16$ shown in figure 7(*a*). Note that the scaling constant is the same as in (3.13). The time at which the tip of the jet pinches off as a drop, $\tilde{t}_p$ is marked by the transition of the full markers into hollow markers, indicating the position of the jet tip and distal side of the drop, respectively. The

gap between both markers, at the moment the drop detaches, corresponds roughly to the drop diameter. From that moment, the newly formed jet tip is tracked simultaneously to the drop location and can be observed as a full marker below each hollow marker. The drop is ejected at a constant speed equal to the jet speed at the moment the drop detaches and travels within the air bubble before impacting the distal bubble side, as observed in the last frame of figure 6(*b*). Once the drop detaches, the retraction at the newly formed jet tip starts forming another bulge of liquid, whose evolution is estimated by subtracting the Taylor–Culick speed from the speed of the jet at the moment the drop detaches $u_j(\tilde{t}_p) - u_{TC}$. This relative speed yields the slope of the drop position corresponding to the dotted lines in figure 7(*a*). Since the retraction of the jet tip is at the origin of the end-pinching breakup of the jet, the volume of the drop ejected from the jet depends on the jet size and retraction speed, but is independent of the jet speed. The drop volume, V_d, is in fact equal to the portion of the jet which has retracted up to the pinch-off time, $\tilde{t}_p$, which can be expressed as

$$V_d = \tilde{t}_p u_{TC} r_j^2 \pi, \tag{3.15}$$

where the jet is approximated as a cylinder of cross-sectional area $r_j^2\pi$. A good correlation between the experiment and (3.15) is observed in the inset of figure 7(*a*).

3.4. *Water-entry of the liquid jet*

The impact of objects such as solid spheres (May & Woodhull 1948; Aristoff & Bush 2009), liquid drops (Engel 1966) or liquid jets (Soh, Khoo & Yuen 2005; Qu *et al.* 2013), normal to an initially quiescent free surface, typically forms a cavity that is driven deeper into the pool by the momentum of the object. Past a certain water-entry velocity, the long narrow cavity surrounding the object collapses from the sides, entrapping a bubble, which pinches off from the end of the cavity and starts journeying in the surrounding water (Oguz, Prosperetti & Kolaini 1995). The entrapment of the bubble can be classified as a shallow seal or a deep seal, depending on the collapse location of the cavity. A shallow seal occurs when the cavity collapses near the free surface, while a deep seal happens when the collapse occurs midway between the tip of the cavity and the free surface. In their pioneering work on shock-induced microbubble dynamics, Ohl & Ikink (2003) have observed the appearance of small daughter bubbles next to the distal side of the gas bubbles right after the passage of a lithotripter shock wave. They have suggested that the water-entry of the shock-induced bubble jets at the distal bubble side, driven by the asymmetrical collapse of the bubble, entrains some gas, which separates from the main bubble. Kersten *et al.* (2003) have proposed that the water-entry of shock-induced micrometre-sized bubble jets is similar to the canonical water-entry of millimetre-sized jets into a flat liquid pool. However, more recently, works on the liquid pool impact of micrometre-sized jets (Speirs *et al.* 2018), still larger than those investigated in the present study, have highlighted some fundamental differences with respect to their millimetre-sized counterparts. Indeed, microjets are characterised by very small Bond numbers, $Bo = \rho g r_j^2/\gamma \sim O(10^{-3})$, where g is the gravitational acceleration, compared with millimetre-sized ones, $Bo > O(10^0)$, indicating that the dynamics of the cavity is not driven by hydrostatic pressure any more but by capillary forces.

Figure 8(*a*,*b*) shows two image sequences of the water-entry of a micrometre-sized jet at the distal side of the bubble, the formation of a cavity and the subsequent pinch-off of an ejected toroidal bubble for figure 8(*b*). Depending on the speed of the bubble jet, the water-entry at the distal side can happen right at the beginning of the expansion phase, or later, when the bubble comes close to reaching its maximum size. Therefore, the relative

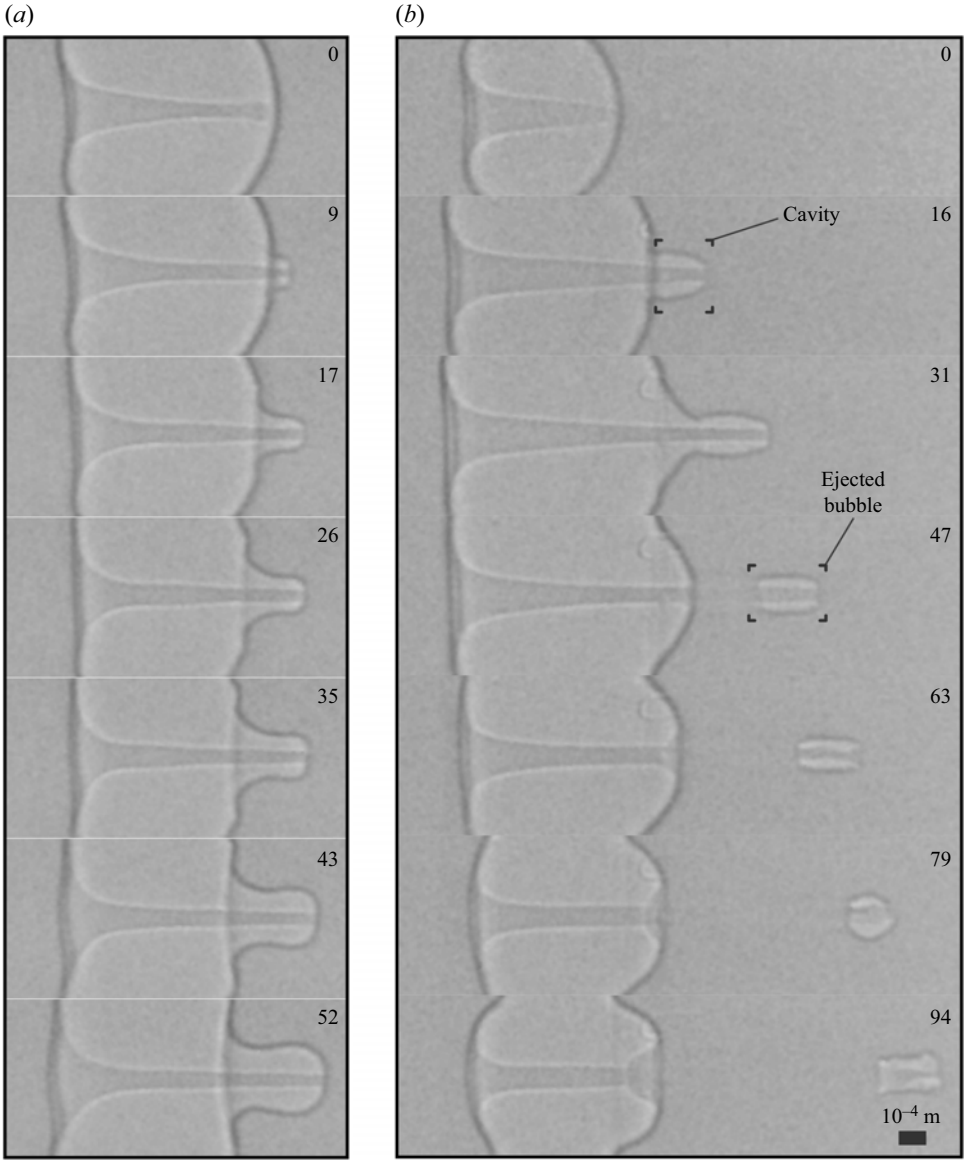

Figure 8. Image sequences of the water entry of shock-induced bubble jets, where (*a*) the shock wave is characterised by a pressure impulse of $J/(r_0^3\sqrt{p_{b,0}\rho}) = 5.44$, driving a cavity that stays attached to the main bubble and where (*b*) the shock wave is characterised by a pressure impulse of $J/(r_0^3\sqrt{p_{b,0}\rho}) = 8.62$, driving a cavity that detaches in the shape of an ejected toroidal bubble. The normalised rescaled time, $\tilde{t}\Delta u_i/r_j$, is indicated on each frame where $\tilde{t} = t - t_i = 0$ is the time at which the jet impacts the distal bubble side and is (*a*) $t_i = 102$ µs and (*b*) $t_i = 34$ µs; r_j and Δu_i are the jet radius and velocity of the jet relative to the distal bubble side, respectively. The scale bar is the same for both image sequences.

impact velocity of the jet Δu_i is influenced by the bubble's expansion velocity, u_b, where $u_b > 0$ when the bubble is not close to its minimum or maximum size. The velocity of the jet relative to the distal bubble side at the moment of impact, t_i, is defined as $\Delta u_i = u_i - u_b$, where u_i is the jet's impact speed and u_b the distal bubble wall velocity at that time. For figure 8(*a*), the relative jet speed at impact is $\Delta u_i = 7.41$ m s^{-1} and

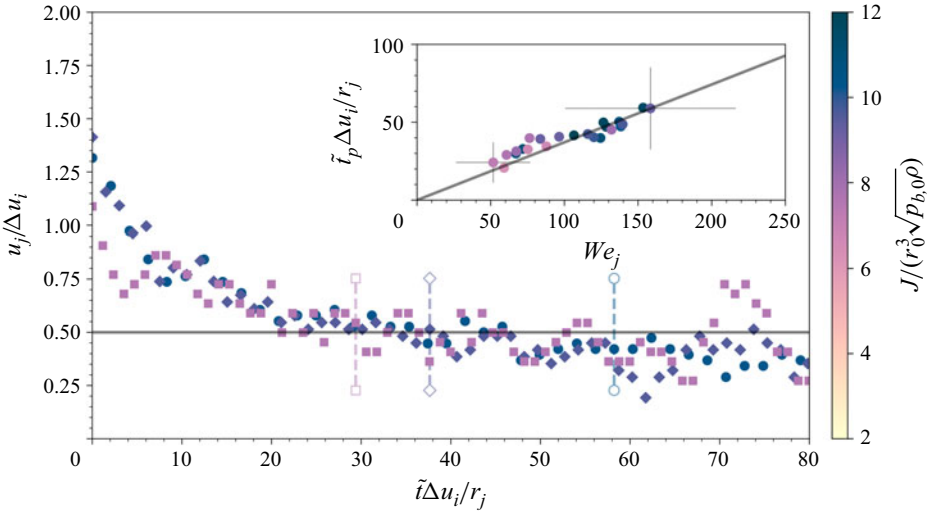

Figure 9. Temporal evolution of the speed of the jet-driven cavity's tip, u_j, from the moment the jet impacts the distal bubble side, $\tilde{t} = t - t_i$. The jet speed and time are normalised to the relative impact speed, $\Delta u_i = u_i - u_b$ and jet radius, r_j. The grey horizontal line indicates $u_j/\Delta u_i = 0.5$ and the dashed vertical lines show the time at which the toroidal bubble pinches off from the tip of the cavity, $\tilde{t}_p$. The impulses are $J/r_0\sqrt{p_{b,0}\rho} =$ 7.52 (□), 9.56 (◇) and 10.31 (○). The inset figure displays the dimensionless pinch-off time against the jet's Weber number, We_j, comparing with the model given by (3.16). Only the minimal and maximal uncertainty are displayed for visual clarity.

the associated Weber number, $We_j = \rho\Delta u_i^2 r_j/\gamma = 15$. For figure 8(*b*), the jet speed is $\Delta u_i = 16.85$ m s^{-1} and the Weber number is $We_j = 88$. The bubble wall velocity is greater for a stronger collapse because the jet reaches the distal side during the bubble's early expansion phase. In contrast, with milder driving, the bubble is close to reaching its maximum size, resulting in a bubble wall velocity close to zero. Immediately after impact, the bubble adopts a torus-like shape and a subsequent toroidal cavity forms, as highlighted in the second frame of figure 8(*b*). In figure 8(*b*), the pinch-off of a toroidal daughter bubble is observable due to the sufficiently high relative jet velocity at the moment of impact. The absence of a pinch-off for figure 8(*a*) is, however, not surprising, given the Weber number associated with this case, which is close to the value of $We_j = 6.8$, where Kersten *et al.* (2003) did not observe pinch-off in their plunging jet experiments. The resulting daughter bubble is indeed toroidal as suggested by Kersten *et al.* (2003).

Figure 9 shows the velocity of the jet tip, which initially coincides with the tip of the cavity as it penetrates the surrounding liquid, and later evolves into the tip of the resulting toroidal bubble. The velocity is normalised to the relative impact velocity, $\Delta u_i = u_i - u_b$, and the time by the characteristic time of the jet, $r_j/\Delta u_i$. The reference frame for time is also modified, where $t = 0$ corresponds to the moment the shock wave impacts the bubble and $\tilde{t} = t - t_i = 0$ to the moment the jet impacts the distal side of the bubble. The temporal evolution of the jet speed is shown for three different shock wave–bubble experiments, with the instant at which a toroidal bubble pinches off from the jet-driven cavity (as visually highlighted in the fourth frame of figure 8*b*) being indicated. The dimensionless speed at which the cavity elongates has been reported to be $u_j/\Delta u_i = 0.5$ for infinitely long millimetre-sized liquid jets (Oguz *et al.* 1995; Speirs *et al.* 2018), although Kersten *et al.* (2003) reported values are in the $u_j/\Delta u_i = 0.6$–0.9 range. Here, after a first phase of deceleration lasting up to $\tilde{t}\Delta u_i/r_j = 25$ for all three test cases, the dimensionless growth

speed of the cavity settles to a constant speed of $u_j/\Delta u_i = 0.5$, as highlighted by the horizontal grey line in figure 9. In fact, the mean and standard deviation for $N = 24$ tests yield a dimensionless speed of the cavity right before pinch-off of the daughter bubble of $u_j/\Delta u_i = 0.51 \pm 0.06$ for the jets of finite length investigated herein. As the tip of the cavity pinches off, the toroidal bubble travels at a speed which slightly decreases, while staying close to $u_j/\Delta u_i = 0.5$ for the duration of the experiment. Fluctuations in the speed of the ejected toroidal bubble are observed because of the deformation of the toroidal bubble. The dimensionless time at which the bubble pinches off from the tip of the cavity, $\tilde{t}_p \Delta u_i / r_j$, grows as the shock wave intensity increases (see vertical lines). The dimensionless pinch-off time is plotted in the inset of figure 9 against the Weber number of the jet at the moment it impacts the distal bubble side. The pinch-off time includes the growth and collapse times of the cavity, which have previously been suggested to scale with We_j^2 (Quetzeri-Santiago *et al.* 2021) and We_j (Kroeze *et al.* 2024), respectively. Here, however, the experimental results indicate a linear dependency on We_j for both the growth and collapse time through the relation

$$\frac{\tilde{t}_p \Delta u_i}{r_j} = G We_j, \tag{3.16}$$

where $G = 0.37$ is a scaling constant fitted to the observations within the parameter range investigated herein.

The pinch-off dynamics following the impact of finite micrometre-sized jets on liquid surfaces is governed by surface tension effects. Therefore, owing to the linear relationship between the jet speed and pressure impulse (Bokman *et al.* 2023), the pinch-off time scales with the pressure impulse of the shock wave as

$$\tilde{t}_p \sim We_j \sim \Delta u_i^2 \sim J^2. \tag{3.17}$$

Kroeze *et al.* (2024) have shown that for jets having a $We_j \leqslant 150$ at impact and a uniform constant velocity from tip to tail, the cavity behaves in the deep seal regime, where the collapse of the cavity around the jet occurs approximately in the middle of the cavity, while Speirs *et al.* (2018) suggest a shallow seal for the same range of Weber number but Bond numbers in the $O(10^{-2})$–$O(10^{-1})$ range. Solely deep seal behaviour is observed in the present work.

As the pinch-off occurs, the X-ray phase contrast images provide a clear quantifiable visual access to the structure of the ejected toroidal bubble. Experiments suggest the outer radius of the toroid to be three times larger than its inner radius. The toroidal bubble's volume can easily be computed, assuming symmetry along the jet axis, by measuring the area of the lobe, A_{lobe}, and its average radius, r_{lobe}, which yields $V = 2\pi r_{lobe} A_{lobe}$. Figure 10(*a*) displays the volume of the ejected toroidal bubble at the moment of pinch-off. The volume is in the nanolitre range for different shock wave drivings and suggests a linear relationship with the relative impact speed of the jet on the distal bubble side. A simple model can easily be derived by assuming that the cavity promptly converges to its constant growth speed of $u_j = \Delta u_i/2$, that the toroidal bubble pinches off at the centre of the deep cavity formed by the jet, and therefore, its length equals half of the cavity's length $l_e = l_c/2$, and that the outer radius of the cavity is $3r_j$. These assumptions, combined with (3.16) and the scaling proposed in (3.17), yield the following relation relating the

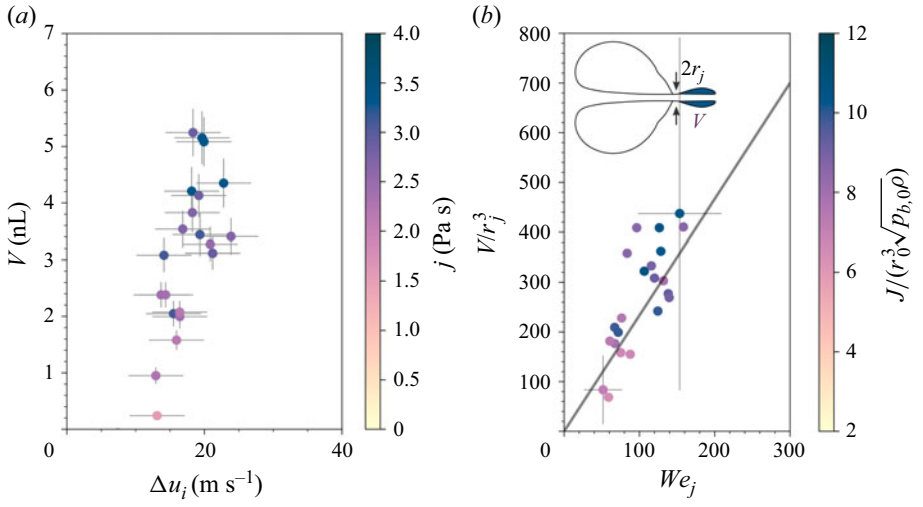

Figure 10. (*a*) Ejected toroidal bubble volume, V, against the relative impact speed of the jet upon water entry, $\Delta u_i = u_i - u_b$. (*b*) Dimensionless volume of the ejected gas bubble against the jet's Weber number upon impact. The grey line displays (3.18). Only the minimal and maximal uncertainty are shown for visual clarity.

ejected volume with the shock wave impulse:

$$\frac{V}{r_j^3} = \frac{\pi\left[(3r_j)^2 - r_j^2\right] l_c}{2r_j^3} = \frac{\pi 8 r_j^2 \tilde{t}_p \Delta u_i}{4r_j^3} = G2\pi\, We_j \sim G2\pi\, J^2. \tag{3.18}$$

The model is compared with experiments in figure 10(*b*) yielding a fairly good estimate of the dimensionless volume at the moment of pinch-off. However, the data are plagued by significant uncertainty caused by the very small jet radii, which are in the 16–32 μm range and therefore approaching resolution limits. Nevertheless, these findings suggest that the volume of the ejected gas can be controlled through the shock wave impulse, which could have implications in technologies such as needle-free injections of nanoaerosols (Hindle & Longest 2010).

4. Conclusion

In this work, the interaction of micrometre-sized air bubbles with impulsive laser-induced shock waves has been examined in detail using X-ray phase contrast imaging, which allows access to all phase discontinuities along the X-ray beam path. The bubble collapse, jet formation, propagation within the bubble and air entrainment as the jet enters the surrounding liquid are visualised, displaying a rich variety of dynamical processes. The undistorted access to the jet within the bubble allows the jet tip evolution, and consequently its speed, to be assessed over time.

The jetting dynamics is investigated from a bubble collapse and interfacial instability perspective. Air bubbles interacting with underwater shock waves have been investigated from a bubble collapse perspective, with equations such as the Rayleigh–Plesset or Keller–Miksis equations. However, while the Rayleigh–Plesset and Keller–Miksis equations effectively capture the volumetric oscillations of a bubble, they assume spherical symmetry and thus fall short in describing jet formation and other asymmetric dynamics.

They can be leveraged to estimate the mean velocity and acceleration of the jet during the collapse of the bubble, based on the bubble collapse time and only to a certain degree of accuracy. Nonetheless, they can provide valuable insights on whether a jet will form or not following the impact of a bubble with a shock wave. The appearance of a jet is found to be a function of the mean acceleration of the bubble during its collapse, where a positive or negative value results in the presence or absence of jets, respectively. The dimensionless mean acceleration is found to scale with the square of the dimensionless pressure impulse applied by the shock wave on the bubble surface. A minimum mean acceleration of the bubble necessary for an instability to grow after its collapse is found for the bubbles investigated in this work, beyond which jets are stable and reach the distal bubble side. The relationship between jetting and acceleration further suggests that shock-induced bubble jets are an acceleration-driven interfacial instability, such as the Rayleigh–Taylor or Richtmyer–Meshkov instability. The jets, when present, can also be described by the Richtmyer–Meshkov instability, the shock-driven impulsive Rayleigh–Taylor instability, by considering the bubbles as quasi-single-mode perturbations. The growth rate of the perturbation, or jet speed, can be described through time thanks to established theory. During the collapse phase of the bubble, the flow equation can be expanded to second order, which yields a linear relationship of the early-time jet speed. A nonlinear decay of the jet speed is observed during the bubble expansion, in conformity with previous findings, and a heuristic formulation based on previous work is derived. A good agreement between the heuristic model and experiments is found from the moment the shock interacts with the bubble, up to the moment the jet merges with the surrounding liquid at the distal bubble side. Application of the heuristic model to the full single-mode perturbation appears to provide a reasonable approximation of the jet shape following its penetration into the bubble.

At the limit of jetting, the jets are found to become unstable due to capillary forces, which may lead to the end-pinching phenomenon, the Rayleigh–Plateau instability for semifinite ligaments. The relative distance of the jet is found to scale with the inertial time scale once the jet's Weber number drops bellow one. Once the capillary forces become dominant, the jet position scales with the capillary time scale. At the jet tip, the inertial pressure of the liquid fails to balance the pressure from interface curvature, leading to ligament retraction at the constant Taylor–Culick speed, which in turn results in liquid accumulating as a bulge that eventually forms a neck and collapses, separating a drop from the jet tip. The ejected drop travels towards the distal bubble side at a constant velocity, and its volume is a function of the Taylor–Culick speed.

The penetration of the jets at the distal bubble side is also observed and found to entrain some gas which eventually detaches from the main bubble in the shape of a toroidal bubble, confirming previous findings (Ohl & Ikink 2003; Kersten *et al.* 2003). The terminal speed of the entrained gas converges to half the relative jet impact speed, and the dimensionless pinch-off time scales linearly with the jet's Weber number for an experimental range which complements previous research on the water-entry of micrometre-sized jets (Kroeze *et al.* 2024). A simple linear relationship between the dimensionless volume of the ejected toroidal bubble and the jet's Weber number at the moment of impact is observed.

The present work provides a wide outlook on shock-induced bubble dynamics in water. It provides fundamental insights into shock wave–bubble interactions at the micrometre scale by linking classic interfacial phenomena, such as cavitation bubble collapse, acceleration- and capillary-driven instabilities and jet penetration, with established theories. By examining these processes at small temporal and spatial scales, the study offers a fresh perspective that unites various traditional models. The proposed use of acceleration-driven instability theory adds a novel dimension to liquid jet modelling,

where understanding stability can allow for precise control of jet initiation (and mitigation) based on initial shock intensities, with potential applications in ICF. Additionally, by investigating the entry of micrometre-sized jets into the surrounding liquid, this research expands on recent findings, with practical implications for applications such as needle-free injections and sonoporation.

Supplementary movies. Supplementary movies are available at https://doi.org/10.1017/jfm.2025.10504.

Funding. The authors acknowledge the financial support from ETH Zurich, the ETH Zurich Postdoctoral Fellowship programme and access to beamtime at beamline ID19 of the ESRF in the frame of the Shock BAG MI1397. This work was performed under the auspices of the US Department of Energy by Lawrence Livermore National Laboratory under Contract DE-AC52-07NA27344.

Declaration of interests. The authors report no conflict of interest.

Data availability statement. The data that support the findings of this study are available under reasonable request.

References

Abe, A., Wang, J., Shioda, M. & Maeno, S. 2015 Observation and analysis of interactive phenomena between microbubbles and underwater shock wave. *J. Vis.* **18** (3), 437–447.

Alon, U., Hecht, J., Ofer, D. & Shvarts, D. 1995 Power laws and similarity of Rayleigh–Taylor and Richtmyer–Meshkov mixing fronts at all density ratios. *Phys. Rev. Lett.* **74** (4), 534.

Antkowiak, A., Bremond, N., Le Dizès, S. & Villermaux, E. 2007 Short-term dynamics of a density interface following an impact. *J. Fluid Mech.* **577**, 241–250.

Apfel, R.E. 1982 Acoustic cavitation: a possible consequence of biomedical uses of ultrasound. *Br. J. Cancer* **5**, 140.

Aristoff, J.M. & Bush, J.W.M. 2009 Water entry of small hydrophobic spheres. *J. Fluid Mech.* **619**, 45–78.

Bekeredjian, R., Bohris, C., Hansen, A., Katus, H.A., Kuecherer, H.F. & Hardt, S.E. 2007 Impact of microbubbles on shock wave-mediated DNA uptake in cells in vitro. *Ultrasound Med. Biol.* **33** (5), 743–750.

Betney, M.R., Tully, B., Hawker, N.A. & Ventikos, Y. 2015 Computational modelling of the interaction of shock waves with multiple gas-filled bubbles in a liquid. *Phys. Fluids* **27** (3), 036101.

Betti, R. & Hurricane, O.A. 2016 Inertial-confinement fusion with lasers. *Nat. Phys.* **12** (5), 435–448.

Birkhoff, G. 1954 Note on Taylor instability. *Q. Appl. Maths* **12** (3), 306–309.

Bokman, G.T., Biasiori-Poulanges, L., Lukić, B., Schmidmayer, K., Bourquard, C., Baumann, E., Rack, A., Olson, B.J. & Supponen, O. 2024 Impulse-driven release of gas-encapsulated drops. *J. Fluid Mech.* **1001**, A51.

Bokman, G.T., Biasiori-Poulanges, L., Meyer, D.W. & Supponen, O. 2023 Scaling laws for bubble collapse driven by an impulsive shock wave. *J. Fluid Mech.* **967**, A33.

Bourne, N.K. & Field, J.E. 1992 Shock-induced collapse of single cavities in liquids. *J. Fluid Mech.* **244**, 225–240.

Brennen, C.E. 2014 *Cavitation and Bubble Dynamics*. Cambridge University Press.

Brenner, M.P., Hilgenfeldt, S. & Lohse, D. 2002 Single-bubble sonoluminescence. *Rev. Mod. Phys.* **74**, 425–484.

Brouillette, M. 2002 The Richtmyer–Meshkov instability. *Annu. Rev. Fluid Mech.* **34** (2002), 445–468.

Calvisi, M.L., Lindau, O., Blake, J.R. & Szeri, A.J. 2007 Shape stability and violent collapse of microbubbles in acoustic traveling waves. *Phys. Fluids* **19** (4), 047101.

Carlès, P. & Popinet, S. 2002 The effect of viscosity, surface tension and non-linearity on Richtmyer–Meshkov instability. *Eur. J. Mech. B Fluids* **21** (5), 511–526.

Castrejón-Pita, A.A., Castrejón-Pita, J.R. & Hutchings, I.M. 2012 Breakup of liquid filaments. *Phys. Rev. Lett.* **108** (7), 074506.

Cloetens, P., Barrett, R., Baruchel, J., Guigay, J.-P. & Schlenker, M. 1996 Phase objects in synchrotron radiation hard x-ray imaging. *J. Phys. D: Appl. Phys.* **29** (1), 133.

Culick, F.E.C. 1960 Comments on a ruptured soap film. *J. Appl. Phys.* **31** (6), 1128–1129.

Davy, B.A. & Blackstock, D.T. 1971 Measurements of the refraction and diffraction of a short n wave by a gas-filled soap bubble. *J. Acoust. Soc. Am.* **49** (3B), 732–737.

Dear, J.P. & Field, J.E. 1988 A study of the collapse of arrays of cavities. *J. Fluid Mech.* **190**, 409–425.

DEAR, J.P., FIELD, J.E. & WALTON, A.J. 1988 Gas compression and jet formation in cavities collapsed by a shock wave. *Nature* **332** (6164), 505–508.
DELIUS, M. & ADAMS, G. 1999 Shock wave permeabilization with ribosome inactivating proteins: a new approach to tumor Therapy1. *Cancer Res.* **59** (20), 5227–5232.
DHOTE, Y., KUMAR, A., KAYAL, L., GOSWAMI, P.S. & DASGUPTA, R. 2024 Standing waves and jets on a sessile, incompressible bubble. *Phys. Fluids* **36** (1), 012105.
DIMONTE, G. & RAMAPRABHU, P. 2010 Simulations and model of the nonlinear Richtmyer–Meshkov instability. *Phys. Fluids* **22** (1), 014104.
DING, Z. & GRACEWSKI, S.M. 1996 The behaviour of a gas cavity impacted by a weak or strong shock wave. *J. Fluid Mech.* **309**, 183–209.
DRAKE, R.P. 2011 Spkie penetration in blast-wave-driven instabilities. *Astrophys. J.* **744** (2), 184.
EGGERS, J. & VILLERMAUX, E. 2008 Physics of liquid jets. *Rep. Prog. Phys.* **71** (3), 036601.
ENGEL, O.G. 1966 Crater depth in fluid impacts. *J. Appl. Phys.* **37** (4), 1798–1808.
FREUND, J.B., SHUKLA, R.K. & EVAN, A.P. 2009 Shock-induced bubble jetting into a viscous fluid with application to tissue injury in shock-wave lithotripsy. *J. Acoust. Soc. Am.* **126** (5), 2746–2756.
GORDILLO, J.M., ONUKI, H. & TAGAWA, Y. 2020 Impulsive generation of jets by flow focusing. *J. Fluid Mech.* **894**, A3.
HAAN, S.W. 1991 Weakly nonlinear hydrodynamic instabilities in inertial fusion. *Phys. Fluids B* **3** (8), 2349–2355.
HAAS, J.-F. & STURTEVANT, B. 1987 Interaction of weak shock waves with cylindrical and spherical gas inhomogeneities. *J. Fluid Mech.* **181**, 41–76.
HINDLE, M. & LONGEST, P.W. 2010 Evaluation of enhanced condensational growth (ECG) for controlled respiratory drug delivery in a mouth-throat and upper tracheobronchial model. *Pharmaceut. Res.* **27**, 1800–1811.
HURRICANE, O.A., PATEL, P.K., BETTI, R., FROULA, D.H., REGAN, S.P., SLUTZ, S.A., GOMEZ, M.R. & SWEENEY, M.A. 2023 Physics principles of inertial confinement fusion and us program overview. *Rev. Mod. Phys.* **95** (2), 025005.
JOHNSEN, E. & COLONIUS, T. 2008 Shock-induced collapse of a gas bubble in shockwave lithotripsy. *J. Acoust. Soc. Am.* **124** (4), 2011–2020.
JOHNSEN, E. & COLONIUS, T. 2009 Numerical simulations of non-spherical bubble collapse. *J. Fluid Mech.* **629**, 231–262.
KELLER, J.B. & MIKSIS, M. 1980 Bubble oscillations of large amplitude. *J. Acoust. Soc. Am.* **68** (2), 628–633.
KERSTEN, B., OHL, C.-D. & PROSPERETTI, A. 2003 Transient impact of a liquid column on a miscible liquid surface. *Phys. Fluids* **15** (3), 821–824.
KLASEBOER, E., FONG, S.-W., TURANGAN, C.K., KHOO, B.C., SZERI, A.J., CALVISI, M.L., SANKIN, G.N. & ZHONG, P. 2007 Interaction of lithotripter shockwaves with single inertial cavitation bubbles. *J. Fluid Mech.* **593**, 33–56.
KOBAYASHI, K., KODAMA, T. & TAKAHIRA, H. 2011 Shock wave–bubble interaction near soft and rigid boundaries during lithotripsy: numerical analysis by the improved ghost fluid method. *Phys. Med. Biol.* **56** (19), 6421–6440.
KODAMA, T. & TAKAYAMA, K. 1998 Dynamic behavior of bubbles during extracorporeal shock-wave lithotripsy. *Ultrasound Med. Biol.* **24** (5), 723–738.
KOUKAS, E., PAPOUTSAKIS, A. & GAVAISES, M. 2023 Numerical investigation of shock-induced bubble collapse dynamics and fluid–solid interactions during shock-wave lithotripsy. *Ultrason. Sonochem.* **95**, 106393.
KROEZE, T.B., FERNANDEZ RIVAS, D. & QUETZERI-SANTIAGO, M.A. 2024 Microfluidic jet impacts on deep pools: transition from capillary-dominated cavity closure to gas-pressure-dominated closure at higher weber numbers. *J. Fluid Mech.* **986**, A24.
KULL, H.-J. 1991 Theory of the Rayleigh–Taylor instability. *Phys. Rep.* **206** (5), 197–325.
KURANZ, C.C., *et al.* 2009 Three-dimensional blast-wave-driven Rayleigh–Taylor instability and the effects of long-wavelength modes. *Phys. Plasmas* **16** (5), 056310.
LAUTERBORN, W. & BOLLE, H. 1975 Experimental investigations of cavitation-bubble collapse in the neighbourhood of a solid boundary. *J. Fluid Mech.* **72** (2), 391–399.
LAUTERBORN, W. & VOGEL, A. 2013 Shock wave emission by laser generated bubbles. In *Bubble Dynamics and Shock Waves*, pp. 67–103. Springer.
LAYES, G., JOURDAN, G. & HOUAS, L. 2009 Experimental study on a plane shock wave accelerating a gas bubble. *Phys. Fluids* **21** (7), 074102.
LAYZER, D. 1955 On the instability of superposed fluids in a gravitational field. *Astrophys. J.* **122**, 1.

Le Gac, S., Zwaan, E., Van Den Berg, A. & Ohl, C.-D. 2007 Sonoporation of suspension cells with a single cavitation bubble in a microfluidic confinement. *Lab on a Chip* **7** (12), 1666–1672.
Li, X.L. & Zhang, Q. 1997 A comparative numerical study of the Richtmyer–Meshkov instability with nonlinear analysis in two and three dimensions. *Phys. Fluids* **9** (10), 3069–3077.
Liang, Y., Zhai, Z., Ding, J. & Luo, X. 2019 Richtmyer–Meshkov instability on a quasi-single-mode interface. *J. Fluid Mech.* **872**, 729–751.
Ligrani, P.M., McNabb, E.S., Collopy, H., Anderson, M. & Marko, S.M. 2020 Recent investigations of shock wave effects and interactions. *Adv. Aerodyn.* **2** (1), 4.
Loske, A.M. 2017 *Medical and Biomedical Applications of Shock Waves*. Springer.
Lui, H.F.S., Ricciardi, T.R., Wolf, W.R., Braun, J., Rahbari, I. & Paniagua, G. 2022 Unsteadiness of shock-boundary layer interactions in a Mach 2.0 supersonic turbine cascade. *Phys. Rev. Fluids* **7**, 094602.
Mason, T.J. 2016 Ultrasonic cleaning: an historical perspective. *Ultrason. Sonochem.* **29**, 519–523.
May, A. & Woodhull, J.C. 1948 Drag coefficients of steel spheres entering water vertically. *J. Appl. Phys.* **19** (12), 1109–1121.
Mikaelian, K.O. 1990 Rayleigh–Taylor and Richtmyer–Meshkov instabilities in multilayer fluids with surface tension. *Phys. Rev. A* **42**, 7211–7225.
Mikaelian, K.O. 2008 Limitations and failures of the Layzer model for hydrodynamic instabilities. *Phys. Rev. E* **78**, 015303.
Mikaelian, K.O. 2014 Solution to Rayleigh–Taylor instabilities: bubbles, spikes, and their scalings. *Phys. Rev. E* **89** (5), 053009.
Oguz, H.N., Prosperetti, A. & Kolaini, A.R. 1995 Air entrapment by a falling water mass. *J. Fluid Mech.* **294**, 181–207.
Ohl, C.D. 2002 Cavitation inception following shock wave passage. *Phys. Fluids* **14** (10), 3512–3521.
Ohl, C.-D., Arora, M., Ikink, R., de Jong, N., Versluis, M., Delius, M. & Lohse, D. 2006 Sonoporation from jetting cavitation bubbles. *Biophys. J.* **91** (11), 4285–4295.
Ohl, C.-D. & Ikink, R. 2003 Shock-wave-induced jetting of micron-size bubbles. *Phys. Rev. Lett.* **90**, 214502.
Ohl, S.-W., Klaseboer, E. & Khoo, B.C. 2015 Bubbles with shock waves and ultrasound: a review. *Interface Focus* **5** (5), 20150019.
Paré, G.N. 2015 Création et éjection des gouttes de l'atomisation *PhD thesis*. Université Pierre et Marie Curie, France.
Petit, B., Bohren, Y., Gaud, E., Bussat, P., Arditi, M., Yan, F., Tranquart, F. & Allémann, E. 2015 Sonothrombolysis: the contribution of stable and inertial cavitation to clot lysis. *Ultrasound Med. Biol.* **41** (5), 1402–1410.
Philipp, A., Delius, M., Scheffczyk, C., Vogel, A. & Lauterborn, W. 1993 Interaction of lithotripter generated shock waves with air bubbles. *J. Acoust. Soc. Am.* **93** (5), 2496–2509.
Plesset, M.S. 1949 The dynamics of cavitation bubbles. *J. Appl. Mech.* **16** (3), 277–282.
Plesset, M.S. & Chapman, R.B. 1971 Collapse of an initially spherical vapour cavity in the neighbourhood of a solid boundary. *J. Fluid Mech.* **47** (2), 283–290.
Plesset, M.S. & Mitchell, T.P. 1956 On the stability of the spherical shape of a vapor cavity in a liquid. *Q. Appl. Maths* **13** (4), 419–430.
Plesset, M.S. & Prosperetti, A. 1977 Bubble dynamics and cavitation. *Annu. Rev. Fluid Mech.* **9** (1977), 145–185.
Prausnitz, M.R., Mitragotri, S. & Langer, R. 2004 Current status and future potential of transdermal drug delivery. *Nat. Rev. Drug Discov.* **3** (2), 115–124.
Qu, X., Goharzadeh, A., Khezzar, L. & Molki, A. 2013 Experimental characterization of air-entrainment in a plunging jet. *Expl Therm. Fluid Sci.* **44**, 51–61.
Quetzeri-Santiago, M.A., Hunter, I.W., Van Der Meer, D. & Fernandez Rivas, D. 2021 Impact of a microfluidic jet on a pendant droplet. *Soft Matt.* **17**, 7466–7475.
Ranjan, D., Niederhaus, J., Motl, B., Anderson, M., Oakley, J. & Bonazza, R. 2007 Experimental investigation of primary and secondary features in high-mach-number shock-bubble interaction. *Phys. Rev. Lett.* **98** (2), 024502.
Ranjan, D., Oakley, J. & Bonazza, R. 2011 Shock-bubble interactions. *Annu. Rev. Fluid Mech.* **43** (2011), 117–140.
Rayleigh, Lord 1917 Viii. on the pressure developed in a liquid during the collapse of a spherical cavity. *Lond. Edinb. Dublin Phil. Mag. J. Sci.* **34** (200), 94–98.
Richtmyer, R.D. 1954 Taylor instability in shock acceleration of compressible fluids. *Tech. Rep*, Los Alamos Scientific Lab.
Rudinger, G. & Somers, L.M. 1960 Behaviour of small regions of different gases carried in accelerated gas flows. *J. Fluid Mech.* **7** (2), 161–176.

SACKMANN, M., *et al.* 1988 Shock-wave lithotripsy of gallbladder stones. *New Engl. J. Med.* **318** (7), 393–397.
SADOT, O., EREZ, L., ALON, U., ORON, D., LEVIN, L.A., EREZ, G., BEN-DOR, G. & SHVARTS, D. 1998 Study of nonlinear evolution of single-mode and two-bubble interaction under Richtmyer–Meshkov instability. *Phys. Rev. Lett.* **80**, 1654–1657.
SHIMA, A., TOMITA, Y. & TAKAHASHI, K. 1984 The collapse of a gas bubble near a solid wall by a shock wave and the induced impulsive pressure. *Proc. Inst. Mech. Engrs C: J. Mech. Engng Sci.* **198** (2), 81–86.
SOH, W.K., KHOO, B.C. & YUEN, D.W.Y. 2005 The entrainment of air by water jet impinging on a free surface. *Exp. Fluids* **39** (3), 498–506.
SOHN, S.-I. 2009 Effects of surface tension and viscosity on the growth rates of Rayleigh–Taylor and Richtmyer–Meshkov instabilities. *Phys. Rev. E: Stat. Nonlin. Soft Matt. Phys.* **80** (5), 055302.
SPEIRS, N.B., PAN, Z., BELDEN, J. & TRUSCOTT, T.T. 2018 The water entry of multi-droplet streams and jets. *J. Fluid Mech.* **844**, 1084–1111.
STONE, H.A. & LEAL, G.L. 1989 Relaxation and breakup of an initially extended drop in an otherwise quiescent fluid. *J. Fluid Mech.* **198**, 399–427.
SUPPONEN, O., OBRESCHKOW, D., TINGUELY, M., KOBEL, P., DORSAZ, N. & FARHAT, M. 2016 Scaling laws for jets of single cavitation bubbles. *J. Fluid Mech.* **802**, 263–293.
TAGAWA, Y., YAMAMOTO, S., HAYASAKA, K. & KAMEDA, M. 2016 On pressure impulse of a laser-induced underwater shock wave. *J. Fluid Mech.* **808**, 5–18.
TANG, K., MOSTERT, W., FUSTER, D. & DEIKE, L. 2021 Effects of surface tension on the Richtmyer–Meshkov instability in fully compressible and inviscid fluids. *Phys. Rev. Fluids* **6**, 113901.
TOMITA, Y. & SHIMA, A. 1986 Mechanisms of impulsive pressure generation and damage pit formation by bubble collapse. *J. Fluid Mech.* **169**, 535–564.
VANDENBOOMGAERDE, M., MÜGLER, C. & GAUTHIER, S. 1998 Impulsive model for the Richtmyer–Meshkov instability. *Phys. Rev. E* **58**, 1874–1882.
VELIKOVICH, A.L., SCHMITT, A.J., GARDNER, J.H. & METZLER, N. 2001 Feedout and Richtmyer–Meshkov instability at large density difference. *Phys. Plasmas* **8** (2), 592–605.
WILKINS, S.W., GUREYEV, T.E., GAO, D., POGANY, A. & STEVENSON, A.W. 1996 Phase-contrast imaging using polychromatic hard X-rays. *Nature* **384** (6607), 335–338.
WOLFRUM, B., KURZ, T., METTIN, R. & LAUTERBORN, W. 2003 Shock wave induced interaction of microbubbles and boundaries. *Phys. Fluids* **15** (10), 2916–2922.
WOUCHUK, J.G. 2001 Growth rate of the linear Richtmyer–Meshkov instability when a shock is reflected. *Phys. Rev. E* **63**, 056303.
YANG, Y., ZHANG, Q. & SHARP, D.H. 1994 Small amplitude theory of Richtmyer–Meshkov instability. *Phys. Fluids* **6** (5), 1856–1873.
ZEFF, B.W., KLEBER, B., FINEBERG, J. & LATHROP, D.P. 2000 Singularity dynamics in curvature collapse and jet eruption on a fluid surface. *Nature* **403** (6768), 401–404.
ZHAI, Z., SI, T., LUO, X. & YANG, J. 2011 On the evolution of spherical gas interfaces accelerated by a planar shock wave. *Phys. Fluids* **23** (8), 084104.
ZHAI, Z., ZOU, L., WU, Q. & LUO, X. 2018 Review of experimental richtmyer–Meshkov instability in shock tube: from simple to complex. *Proc. Inst. Mech. Engrs C: J. Mech. Engng Sci.* **232** (16), 2830–2849.
ZHANG, Q. 1998 Analytical solutions of layzer-type approach to unstable interfacial fluid mixing. *Phys. Rev. Lett.* **81** (16), 3391.
ZHANG, Q. & GUO, W. 2016 Universality of finger growth in two-dimensional Rayleigh–Taylor and Richtmyer–Meshkov instabilities with all density ratios. *J. Fluid Mech.* **786**, 47–61.
ZHANG, Q. & SOHN, S.-I. 1996 An analytical nonlinear theory of Richtmyer–Meshkov instability. *Phys. Lett. A* **212** (3), 149–155.
ZHANG, Q. & SOHN, S.I. 1999 Quantitative theory of Richtmyer–Meshkov instability in three dimensions. *Z. Angew. Math. Phys.* **50** (1), 1–46.
ZHONG, P., LIN, H., XI, X., ZHU, S. & BHOGTE, E.S. 1999 Shock wave–inertial microbubble interaction: methodology, physical characterization, and bioeffect study. *J. Acoust. Soc. Am.* **105** (3), 1997–2009.
ZHOU, Y. 2017 Rayleigh–Taylor and Richtmyer–Meshkov instability induced flow, turbulence, and mixing. I. *Phys. Rep.* **720-722**, 1–136.
ZHOU, Y., 2021 Rayleigh–Taylor and Richtmyer–Meshkov instabilities: a journey through scales. *Physica D: Nonlinear Phenom.* **423**, 132838.